University of Stuttgart
Institute of Aircraft Design

NASA/ DLR Design Challenge 2019

HyBird Aircraft Concept

Team

Jonas Mangold
Michael Lang
Jonathan Stober
Felix Ladwein
Florian Will

Academic Support and Advisors

Prof. Dr. Andreas Strohmayer
Ingmar Geiß
Johannes Schneider

Institute of Aircraft Design
University of Stuttgart

Submitted on July 1st, 2019

Universität Stuttgart

Institut für Flugzeugbau

Institutsleitung
Prof. Dr. Peter Middendorf
Prof. Dr. Po Wen Cheng
Prof. Dr. Andreas Strohmayer

Universität Stuttgart
Institut für Flugzeugbau • Pfaffenwaldring 31 • 70569 Stuttgart

Kontakt
Ingmar Geiß
Pfaffenwaldring 31
70569 Stuttgart
T 0711 685-60528
F 0711 685-62449
E-Mail:
geiss@ifb.uni-stuttgart.de
www.ifb.uni-stuttgart.de

Betreff: Bestätigungsschreiben

01.07.2019

Sehr geehrte Damen und Herren,

hiermit bestätige ich, dass die im Folgenden aufgeführten Mitglieder des studentischen Teams selbstständig den Flugzeugentwurf zur Teilnahme an der NASA/DLR-Design Challenge 2019 durchgeführt haben.

- Jonas Mangold
- Michael Lang
- Jonathan Stober
- Felix Ladwein
- Florian Will

Mit freundlichen Grüßen,

Ingmar Geiß

Betreuender wissenschaftlicher Mitarbeiter

Team Members

Jonas Mangold, B.Sc.
Master Student: Aerospace Engineering
2nd semester

Preliminary Design, Autonomous Systems and Operations, Project Coordination

Michael Lang, B.Sc.
Master Student: Aerospace Engineering
2nd semester

CAD, System Integration, Propulsion System

Jonathan Stober, B.Sc.
Master Student: Aerospace Engineering
2nd semester

Aerodynamics, Noise, Autonomous System

Felix Ladwein, B.Sc.
Master Student: Aerospace Engineering
2nd semester

Simulation and Optimization, Propulsion Architecture

Florian Will, B.Sc.
Master Student: Aerospace Engineering
4th semester

Mass Calculation, Market and Costs Analysis, Certification

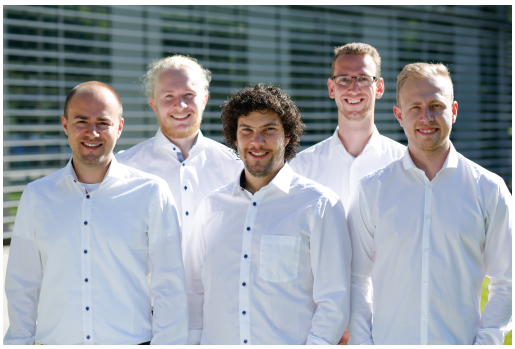

HyBird Team

Abstract

The NASA/DLR Design challenge poses students with the task to develop an efficient 9-seater commuter aircraft that can be easily converted to a cargo configuration. Furthermore, capabilities for autonomous operation and short take-off and landing are required. This design report presents a possible solution to the challenge. Using a combination of well-known design methods and the advantage of today's available computing power makes it possible to evaluate and optimize an unconventional propulsion architecture. The resulting design is an aircraft with a high wing configuration with a Coanda flap system, a V-tail, and conventional fuselage, all made from carbon composites. Placing large electrically driven propellers at the tips of the wing and empennage reduces noise and increases efficiency. A serial hybrid architecture with two turbine generators in the nose of the aircraft powers the electric motors. Switching off one of the turbine generators during cruise increases engine efficiency. In combination with the lightweight structure this decreases the fuel consumption significantly. The maximum range of 380 nm allows the plane to cover over 97 % of the US mainland from the 20 biggest airports with direct operating cost reductions of up to 50% compared to existing aircraft.

Contents

Nomenclature

Abbreviations

AEO	All Engines Operative
CG	Center of Gravity
DLR	German Aerospace Center
DOC	Direct Operating Cost
EAS	Essential Air Service
FAA	Federal Aviation Administration
GPS	Global Positioning System
LD	Landing Distance
LIDAR	Light Detection and Ranging
MLM	Maximum Landing Mass
MTOM	Maximum Take-Off Mass
MTOW	Maximum Take-Off Weight
MZFM	Maximum Zero Fuel Mass
NASA	National Aeronautics and Space Administration
OCD	Obstacle Clear Distance
OEI	One Engine Inoperative
QDF	Quantity Discount Factor
STOL	Short Take-Off and Landing
TOD	Take-Off Distance
TRL	Technology Readiness Level
WHM	Wheel Hub Motor
WTP	Wing Tip Propeller

Symbols

Latin

A	$[-]$	Aspect Ratio
b	[m]	Wing Span
c	[m]	Chord Length
C	$[-]$	Coefficients
d	[m]	Diameter
D	[N]	Drag
F	[N]	Force
h	[ft]	Altitude
J	$[-]$	Coefficient
l	[m]	Landing Distance
L	[N]	Lift
m	[kg]	Mass
M	$[-]$	Mach Number
n	$[\frac{1}{\text{min}}]$	Rotation Speed
p	$[\frac{\text{N}}{\text{m}^2}]$	Pressure
P	[W]	Power
r	[m]	Radius
S	$[\text{m}^2]$	Wing Surface

V	$[-]$	Volume Coefficient
x	[m]	Position

Greek

α	$[^\circ]$	Angle of Attack
γ	$[-]$	Circulation
Γ	$[^\circ]$	Angle
δ	$[^\circ]$	Flap Angle
Δ	$[-]$	Delta (Difference)
λ	$[-]$	Taper Ratio
η	$[-]$	Efficiency
ρ	$[\frac{\text{kg}}{\text{m}^3}]$	Density

Subscripts

D, d	Drag
h	Horizontal
ind	Induced
L, l	Lift
max	Maximum
p	Pressure
P	Power
ref	Reference
v	Vertical

List of Figures

List of Tables

1. Introduction

The commercial use of small aircraft for thin-haul connections currently presents airlines with environmental and financial difficulties. These flight routes are essential for fast connections between rural areas and cities. However, they are often not profitable without subsidization. For example, the US Government has implemented the Essential Air Service Program, which supports small airports and airlines to ensure continued service of these routes [1, 28].

The main task of the NASA/ DLR Design Challenge 2019 [1] is to design an aircraft for the efficient operation of commuter routes. To maximize utilization of the aircraft, it needs to be easily convertible between a passenger configuration (nine people) and a cargo configuration (2000 lbs). Moreover, short take-off and landing (STOL) capabilities are required to increase the number of serviceable airfields. This requirement shows a discrepancy to efficient cruise. Additionally, the aircraft should produce low noise emissions and meet modern environmental standards. The aircraft has to be flown by a single pilot for passenger missions, but an autonomous operation shall be possible for cargo missions and future passenger missions to reduce costs. Therefore, new concepts and technologies have to be considered and merged in a intelligent way to generate synergies and find the best balance between these contrary requirements.

In this report, an aircraft is designed that takes both the current market situation and the design specification into account. For this, technologies are compared and selected to allow entry into service in 2025. The aircraft configuration is optimized by combining computing power with established equations and handbook methods [1].

2. Market Analysis

The goal when developing a new commercial airplane is to create a product that allows the airline to have lower operating costs and to reach new customers, thereby increasing revenue. Improving efficiency usually comes with the penalty of higher development costs, which in turn increases the purchasing price of an aircraft. To still be competitive, the new aircraft must hence provide significant reductions in maintenance costs and direct operation costs (DOC). For example, lowering the yearly maintenance cost by 40 % allows an airline to purchase an aircraft that is three times more expensive than an old generation aircraft. [80].

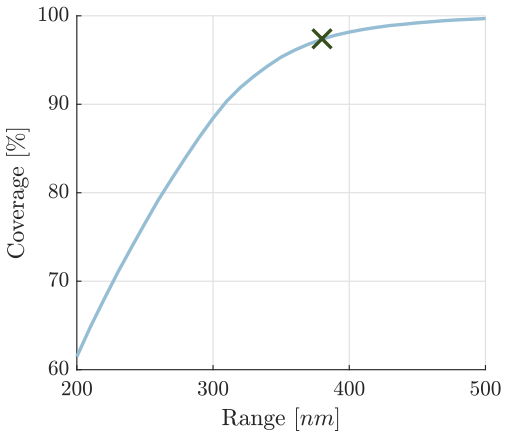

Figure 2.1.: Covered area in the United States over Range

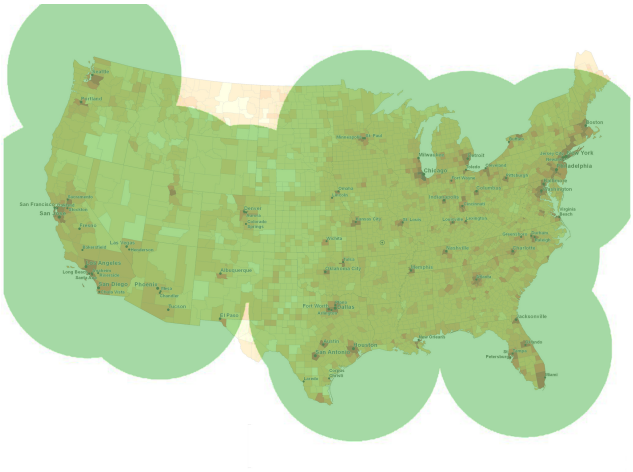

Figure 2.2.: Covered area in the United States from the 20 biggest airports [3]

One factor of the DOCs is fuel consumption, which is also essential from an environmental standpoint. The amount of fuel needed increases exponentially with the range of the aircraft. Having a shorter range directly contradicts the goal to reach more potential customers. There is a worldwide demand for short range commuter aircraft, for example to connect offshore islands to the mainland [51]. However, the largest market for such aircraft is the United States. Currently, all of the routes serviced by the largest

US commuter airline are shorter than 200 nm [70], raising the question of whether designing a longer range aircraft is economically viable. To find the ideal range, the area covered when offering flights from the 20 biggest airports on the US mainland is analyzed. This is done by counting the pixels that fall within the ranges from 200 nm to 500 nm and then plotting the covered area for each range, as shown in Figure 2.1 and Figure 2.2. From this analysis, it is found that selecting a range of 380 nm covers 97 % of the US mainland from the 20 biggest airports.

3. Design Process

The applied design method is presented in Figure 3.1 and is a modification of the established preliminary design approach described by Roskam [59]. It takes advantage of modern computing technology and algorithms to perform design iteration steps digitally instead of manually. After defining the requirements, possible aircraft configurations are generated based on current research and the existing aircraft market [32]. Design sketches are created, and each configuration is evaluated based on its potential to fulfill the requirements, the maturity of the applied technologies and design risks. A total of 15 different aircraft configurations are evaluated, with the most promising being chosen for further analysis. The chosen configuration is described in more detail in the next section. After a similar decision process for the power-plant configuration, the design proceeds to the initial sizing phase. The first mass estimation is carried out by using mass fraction according to Roskam [59], and the required wing area and installed power is determined from the design chart. These values are used as a starting point for a modern enhancement of the design iteration phase. A collection of models and tools that analyze the aircraft configuration and optimize its design parameters is programmed. Evolving from manual iteration of the design using purely analytic equations allows significantly more iterations to be evaluated and multiple parameters simultaneously to be optimized. Moreover, the quality of the preliminary design is improved because the digital models can more accurately represent the characteristics of unconventional configurations. After the digital design optimization, its sensitivity to a variation of key design choices and technical parameters such as battery energy density is investigated. Finally, the design is compared with similar existing aircraft, and the fulfillment of all requirements and design goals is verified.

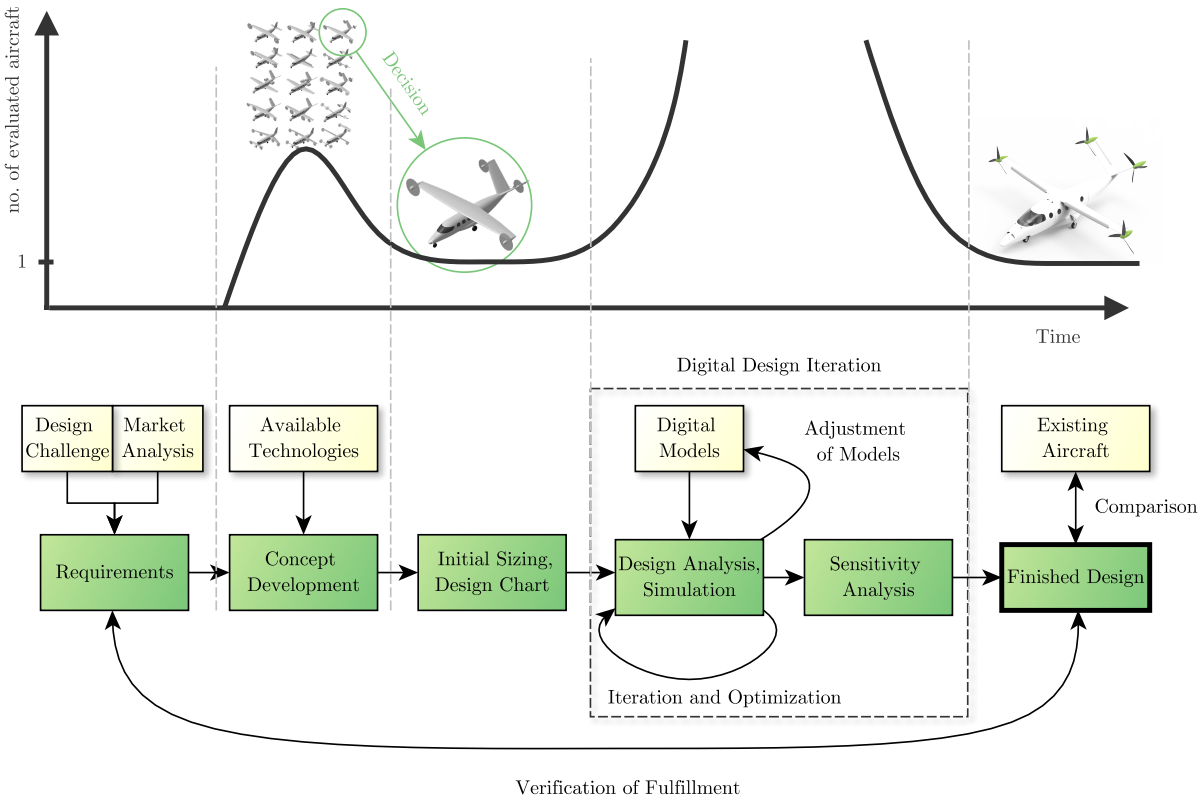

Figure 3.1.: Visualization of the applied design method

3.1. Aircraft Configuration

The chosen aircraft configuration for this design report and the factors contributing to this decision are presented in this section. New aircraft configurations developed in several current research programs aim to take advantage from the new possibilities that arise from the recent improvements in electric motor and battery technology.

Why electric motors? New and optimized electric motors have a much higher specific power than combustion engines. They can be placed almost anywhere on the aircraft due to their compactness at any scale. With proper positioning of the motors, improved propulsive efficiency can be achieved. The electric motor is the ideal option for HyBird because it provides a high power output without an efficiency penalty while also being independent of the power source choice [24].

What is the ideal propeller position? Using electric motors allows for increased freedom in propeller placement, allowing for a wide range of potential propulsion architectures. For small and medium sized aircraft the most prominently discussed concepts are distributed propulsion, wingtip propellers and propellers placed at the tip of the vertical stabilizer [71].
The distributed propulsion concept places numerous propellers at the leading edge of the wing. This increases the wing dynamic pressure and therefore increases the lift coefficient at low-speeds, which in turn allows the wing size to be reduced [46]. It also provides a high failure tolerance [31]. However, there are many open questions regarding this concept, including the mutual influence of the propellers and noise emissions. NASA is currently researching this concept with the X-57 Maxwell experimental plane [26, 35].

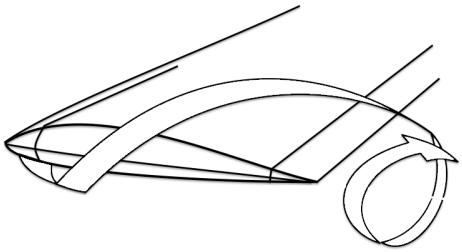

Figure 3.2.: Schematic of a wing tip trailing vortex [41]

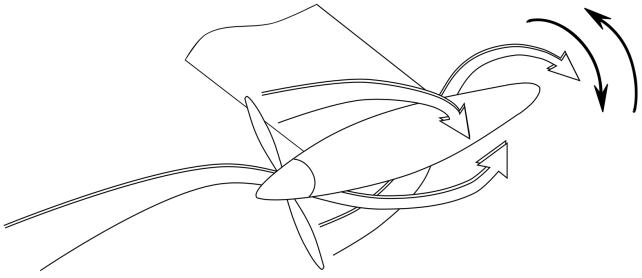

Figure 3.3.: Schematic of the interaction of the wing tip and propeller vortex [66]

Placing large propellers at the wingtips creates a beneficial interaction with the wing tip vortex, which is shown in Figure 3.2 and Figure 3.3. The wing tip vortex is the result of the pressure difference between the upper and lower side of the wing and is the cause of induced drag [65]. According to Patterson, Bartlett and Flechner [49, 50] the energy lost in the wingtip vortex can be partially recovered through the interaction with the propeller, which rotates in the opposite direction of the wing tip vortex. Researchers interpret this energy recovery either as a reduction in induced drag or an increase in effective thrust [41, 49]. In this paper, it is assumed that wing tip propellers increase the effective thrust, which decreases the required power during cruise and climb by 25 % [49].

Compared to the distributed propulsion concept the wingtip propeller concept creates strong yaw moments in case of a single engine failure. However, uninterrupted airflow is achieved across most of the wingspan, which increases laminar flow [11]. The third concept for engine integration has a propeller placed on the vertical stabilizer. This allows for a mostly uninterrupted airflow in front of and behind the propellers, which improves propulsive efficiency. Also, the dynamic pressure at the control surface is raised, which increases its effectiveness [24]. Powered lift concepts such as tilting propellers are not considered a viable option. The reason for this is the

Figure 3.4.: Propeller position on HyBird

increased mechanical complexity, extra power needed, and the risk of an engine failure. Together this leads to a penalty in range and efficiency [42].

Considering the different advantages and disadvantages, a combination of wingtip propellers with vertical stabilizer propellers is chosen for HyBird.

What are the consequences for the wing and control surfaces? For the wing configuration, there are three possible options: a high wing or a low wing in the conventional tailplane configuration, and a canard configuration. The main criteria for the evaluation of the wing positioning are ground clearance of the propellers, accessibility during cargo loading, flight dynamics, aerodynamics, and landing gear integration. A high wing offers the best ground clearance for the wingtip propellers and provides good accessibility for loading while featuring good aerodynamic efficiency and flight dynamics. Landing gear integration generally is more complex than for a low wing, but the overall conclusion is that a high wing is the most favourable configuration for HyBird.

Of the many possible tailplane configurations, the V-tail potentially has the lowest drag. This is due to decreased interference drag and less wetted area. Historically, the main disadvantage of a V-tail has been the difficulty to mechanically mix the elevator and rudder inputs by the pilot. This can be easily solved using modern fly-by-wire systems. Another significant advantage of using a V-tail for HyBird is that it allows for the installation of two large tail propellers, one at each tip, instead of only one propeller at the tip of a conventional vertical stabilizer. Thereby the total propeller area is increased, which increases propulsive efficiency and decreases noise. Furthermore, having two tail propellers results in a higher degree of safety [16].

3.2. Power-Plant

Following the decision on the aircraft configuration, it is necessary to find the the appropriate means to provide power for the electric motors. The power-plant consists of these energy storage and conversion systems.

3.2.1. Comparison of Power-Plant Concepts

The different concepts judged on efficiency, weight, mission scenario applicability, failure tolerance, cost-effectiveness, environmental impact, and technology readiness. The following technologies are considered for HyBird:

- Turboelectric: an internal combustion engine generates shaft power, which is converted to electrical power.
- Serial hybrid: similar to the turboelectric architecture, but including a battery for additional energy storage.
- Battery electric: the only energy storage and power source are batteries.
- Fuel cell: the electric power is produced by a chemical reaction of hydrogen and oxygen.

	Turboelectric	Serial Hybrid	Battery Electric	Fuel Cell
Efficiency	0	+	++	+
Weight	+	+	−−	0
Refueling infrastructure	++	++	−−	−
Failure tolerance	−	0	0	0
Cost-effectiveness,	+	0	−	−
Environmental impact	−−	0	+	++
Technology readiness	+	+	0	0

Table 3.1.: Trade-off study of possible electric power sources; best: ++, worst −−

The advantages and disadvantages for these are shown in Table 3.1. Overall, the serial hybrid concept appears to be the most suited for HyBird, because it offers the best balance of efficiency, weight, costs and availability. It is therefore chosen for HyBird. The following section presents how it is implemented in HyBird.

3.2.2. Power-Plant Configuration

Three possible configurations for a serial hybrid system are evaluated. Firstly, two identical internal combustion engines. Secondly, two different sized engines, and thirdly, one combustion engine. They are evaluated as follows:

1. Two identical internal combustion engines: Using two engines instead of one is advantageous in the case of an engine failure. The power load in this case is split between the remaining combustion engine and the battery, which allows for the installation of a significantly smaller and lighter battery. Additionally, only the maintenance know-how for on type of engine is needed. Another advantage of this configuration is that it allows to switch off one of the combustion engines during phases with less power demand. In this case, the remaining engine runs closer to its optimum load, which increases efficiency and therefore lowers the total fuel consumption. The time between overhaul is also extended when alternating between engines, during cruise
2. Two differently sized engines: in this case the failure of the larger engine would lead to a significant loss in performance. In a situation in which the aircraft is operating at its performance limits, for example, take-off, the power loss could not be compensated
3. Single combustion engine: This would require a far larger battery compared to the other two configuration. The reason for this is that it would have to provide all for the necessary power in a one engine out failure scenario

As a result the power-plant of HyBird, see Figure 3.5, consists of two identical internal combustion engines located in the nose of the aircraft. A rotor burst containment wall separates those engines. Each engine powers a generator which generates the electric power to drive the electric motors and to recharge the battery. The air flow for the turbines comes from two NACA ducts in front of the nose. These inlets are suitable for axial-flow compressors [21] and therefore, are viable for use in HyBird. To counter the wing root bending moment the batteries and the fuel system are installed in the wing behind the wing spars.

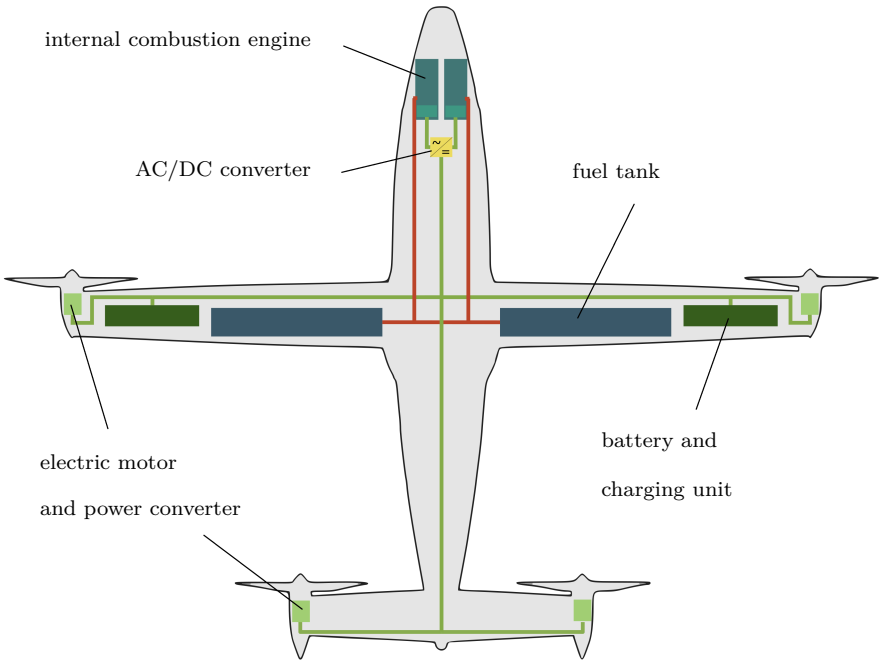

Figure 3.5.: Power-plant configuration installed in HyBird. All systems, power-lines and power-units are installed redundantly and are simplified in the drawing

3.2.3. Internal Combustion Engine Technologies

In addition to conventional diesel and turboshaft engines, a recuperating turbine engine is considered as internal combustion engine for the HyBird. The recuperating turbine engine, an improved turboshaft engine, that converts thermal energy extracted from the hot exhaust gases into electric power. Although there is a weight penalty, the specific fuel consumption is lower compared to a conventional turboshaft engine [70]. All three engine technologies are evaluated in the design iteration phase. This analysis is presented in Chapter 5 of this paper.

3.2.4. Wheel Hub Motor and Electrical Braking

To generate a safer taxi during manual or autonomous operation, wheel-hub motors are installed in the main gear. With these motors, it is possible to handle the aircraft on the ground without any spinning propellers [64]. Additionally, the motors are used to increase the acceleration during take-off, reducing the necessary take-off distance. No hydraulic braking system is needed with this concept, removing the risk of leaks or fire while also reducing the costs to maintain the brake system by 80 %. Nowadays an electric braking system is already installed on the Boeing 787 [40].

3.3. Design Chart

The requirements state that the aircraft has to reach its destination in under 99 minutes. Considering a desired range of 380 nm results in a cruise speed of around 260 knots. According to 14 CFR § 91.117 a) [19], the flight altitude must be over 10,000 ft if the indicated airspeed is more than 250 knots. A cruise altitude of 27,000 ft is chosen, which is a typical value for regional turboprop aircraft. This requires a pressurized cabin. To increase the time spent in efficient cruise, it is desirable to reach the cruise altitude as quickly as possible. Hence, an average climb rate of 2,500 ft/min is chosen. According to CFR 14 Part 23 §23.2120 b)2) [19] a climb gradient of 2 % in a One Engine Inoperative (OEI) case is required. While the American Regulations, 14 CFR Part 23 [19], have no stall speed requirement, the European Certification Specifications CS-23, CS23.49 [18], require a maximum stall speed of 61 knots for single engine aircraft. Although HyBird is a multi engine aircraft, 61 knots is chosen as orientation in order to provide good handling characteristics. This allows for a low approach speed, which is beneficial for short landing distances and reduced noise emissions [38]. Additionally, a Coanda flap systems provides an estimated lift coefficient of $C_L = 4$ (see Section 5.4.2). The take-off and landing distance is set to 700 ft (see Section 4.1). The resulting design chart is shown in Figure 3.6.

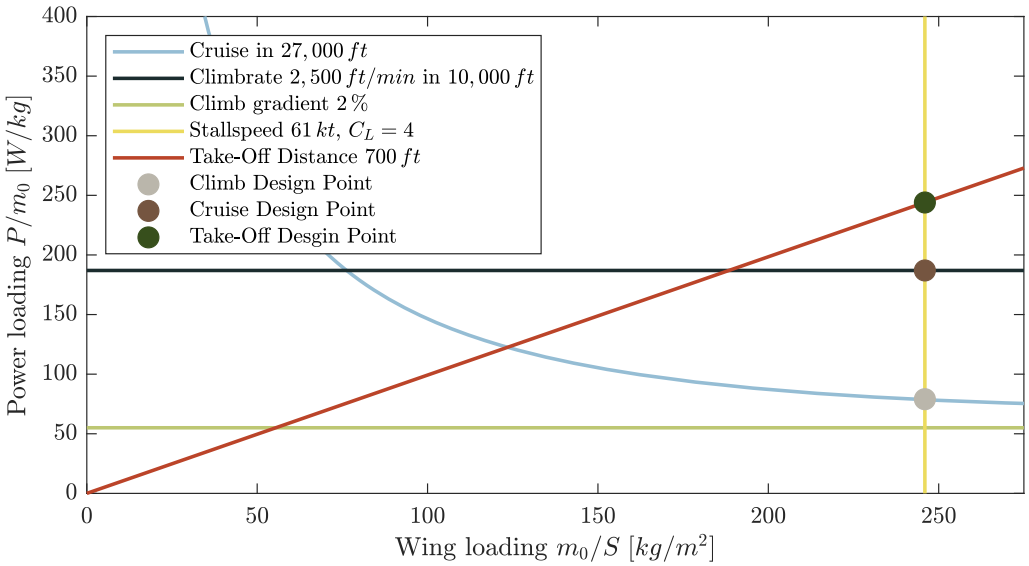

Figure 3.6.: Preliminary Design Chart through resulting design points

The three design points corresponding to the main flight phases are shown in Table 3.2. It is noticeable that the power loading varies significantly between the different points. These different values will affect the sizing of the propulsion system (see Section 5.1).

Design Point	P/m_0 $[W/kg]$	m_0/S $[kg/m^2]$
take-off	244	245
climb	187	245
cruise	79	245

Table 3.2.: Design points and input values for the simulation; showing the wing and power loading

3.4. Cabin Configuration

The cabin of the aircraft is designed to transport up to nine passengers or four US Pallets Type 100 with a total payload of 2000 lb. The European pallets have the same width but are 0.2 m shorter. Thus enabling the carriage of five European pallets. Due to the multi modal utilization of HyBird, the cabin needs to be easily convertible between the passenger and the cargo configuration.

Passenger Configuration (1)

The layout of the cabin in the passenger configuration is a classical commuter layout [32]. To allow the passengers to look outside windows are installed on every seat position. This gives the passengers a more secure feeling [58].

Cargo Configuration (2)

To quickly Load and Unload the aircraft, HyBird features a cargo door which is located 0.2 m behind the trailing edge of the wing. With this position it possible to load and unload the airplane with a forklift at smaller rural airports and with a small cargo or belt loader at larger airports. The floor of the cabin features an aerofilm system, which lifts the cargo using compressed air. The compressed air flows out of small holes, generating a thin film of air to assist in cargo handling. The compressed air comes from the cabin pressure system, which is not needed during loading and unloading [8]. To secure the cargo, there are several hooks on the floor and on the sidewalls. With these hooks it is possible to use all common net and stripe systems used in aviation [15]. The cargo operations are performed autonomously therefore, no pilot is needed and all seats can be stored in the baggage compartment in the rear.

Training Configuration (3)

To have two pilots in the cockpit, the ninth seat assembly can also moved to the co-pilot position. This can be used for training and type rating flights, where a second pilot is necessary. During those kinds of flights no passengers are usually on board.

Additional: Nine Passenger and Two Pilots Configuration (4)

It is also possible to have a nine passenger and two pilot layout in the cabin. This could be used in countries where a second pilot in the cockpit is required for regulatory reasons.

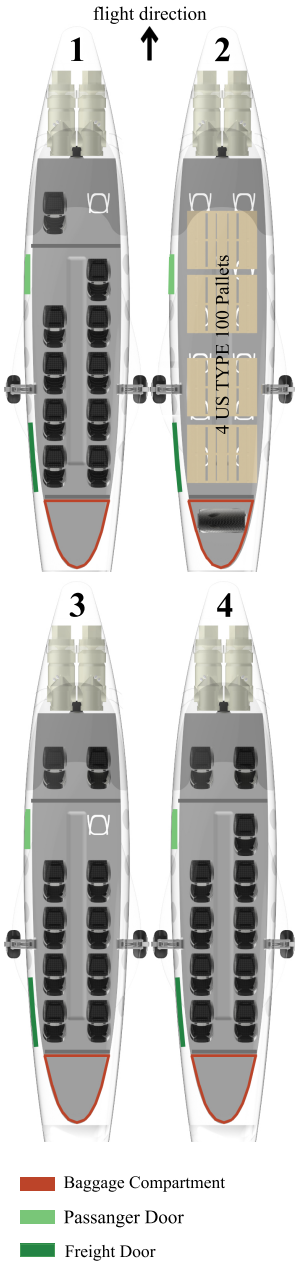

Figure 3.7.: Different cabin configuration

Conversion between Cargo and Passenger Configuration

To achieve the best flexibility for airline customers, the seats are foldable and can be easily removed from the aircraft. During cargo flights, the seats can be stored in the aircraft's luggage compartment, allowing the plane to be quickly converted to a passenger configuration upon arrival. Alternatively, the plane can be flown without the seats, allowing it to carry $80\,kg$ more payload. The seats have two main components: the removable seat-backrest assembly and a frame which is fixed to the airplane floor. The seat assembly can be folded together. The frame can fold flat into the cabin floor [68].

Door and Freight Door

Behind the cockpit is the regular passenger door. The lower part of the door is folded down to create two steps. With this door no extra equipment in needed on the airfield. The freight door at the back is wide enough to load typical European or US Type 100 pallets [37]. Furthermore, additional protection is installed in the loading area in order to prevent damage to the carbon fiber aircraft structure.

3.5. Aircraft Systems

HyBird uses a Fly-by-Wire system, which is industry standard [39]. The actuation system is implemented with electrical actuators and an additional dissimilarity backup system [44]. Qioa et al. [57], describes several advantages for more electric aircraft, which leads to this decision.

3.5.1. Electric Pressurization and Ice Protection

Wing ice protection, cabin pressurization and air conditioning are typically the aircraft systems with the highest power demand. Since HyBird uses a highly electrified propulsion system, it is reasonable to also electrify these systems. The two commonly discussed electric ice protection systems are electrothermic anti-ice systems and electrostatic discharge de-icing systems. The latter has a significantly lower power demand, because it only requires short bursts of electric current compared to the continuous current required for electrothermic heating [72]. Therefore, HyBird will have an electrostatic discharge de-icing system. The power demand for electric cabin pressurization and air conditions greatly depends on the external atmospheric conditions, increasing with higher temperatures or altitudes. By scaling the data from [73] the total required electric systems power is estimated at about $9\,kW$, which is about $4\,\%$ of the electric power required for propulsion during cruise.

3.5.2. Autonomous Flight System

Since HyBird is equipped with fly-by-wire, the computer can control the required actuators and perform flight maneuvers. This is necessary to enable autonomous operation. Because small airports have no instrument landing system, the aircraft must have autonomous landing capabilities onboard. Pinchetti [55] describes the development of a low complexity framework for autonomous landing, take-off, and flight path definition without using any ground-based facilities. Furthermore, all functions are developed deterministically to have reproducibility and accountability compared to a system based on artificial intelligence. Due to the accuracy needed during the final approach and landing phases, only sensors that are independent of other systems are used [54].

GPS The GPS sensors are required to get the position of the aircraft in all three dimensions. These sensors are used during all phases of flight. During climb, cruise, and decent, the accuracy of the GPS-data alone is sufficient. However, for take-off and landing a more accurate sensor is required.

Radar A radar system are needed to check the environment in front of the aircraft for obstacles, including other airplanes. In addition, it measures the altitude, allowing altitude data from the GPS to be verified. Because of its higher accuracy and weather independence, it is used for approach and landing [77, 30]. However, scanning speeds for radar systems are limited, and they may be inefficient for near real-time obstacle and road boundary detection [79].

Light Detection and Ranging Light Detection and Ranging (LIDAR) compensates for low scanning speed of the radar. It is useful for road boundary and obstacle detection [81]. Furthermore, it is working in any case of adverse weather conditions. LIDAR has a resolution of $30\,mm$ at a distance of $80\,m$. A common disadvantage of laser systems is that black obstacles, like water, absorb the light and only weakly reflect the signal. The aircraft operates with a LIDAR system during several phases of the flight, including at altitudes below $35\,ft$ and while taxi and approach. The LIDAR system also uses three-dimensional resolution to check the runway for hazardous obstacles.

Geographical Database A Geographical database must be available onboard that overlaps the sensor data onto a map. Because of inaccuracy in the location of the runway needs to be calibrated to ensure a safe landing. This has been shown through test flights of the research plane of the University of Stuttgart [55]. The calibration of the sensors could be carried out using either an accurately measured GPS data of the runway or by a test flight in which the pilot manually calibrates the map.

Because the fly-by-wire system is already installed, the additional weight of implementing these sensors is negligible as well as the increase in system power. Figure 3.8 illustrates the area coverd by sensors around the plane. The sensor can also support the pilot during passenger missions. Figure 3.9 shows the approach and landing scenarios. All other systems/ sensors are required for redundancy. Additionally, cameras are used to ensure safe ground operations, such as an independent push-back using the wheel hub motors.

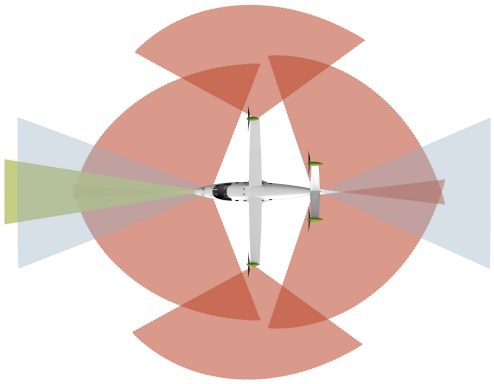

Figure 3.8.: Autonomous systems during taxi: LIDAR (red), camera (blue), radar (green)

Figure 3.9.: Autonomous systems for landing and height detection: LIDAR (red), radar (green), GPS (black)

3.6. Certification

This section gives a brief overview of the main challenges expected during the certification process. HyBird is supposed to be certified according to FAR Part 23 of the FAA regulations. The aircraft includes a number of critical technologies that have not been certified under these regulations before, which are outlined below: First, a serial hybrid that uses two turbines and a battery to provide power to four propellers, to ensure that the power system can compensate for a OEI scenario. Second, the high lift system, see Section 5.4.2, to ensure that the stall speed is below $61\,kts$ as defined in the design chart. Because of these configuration advances, a longer certification process is expected. Three prototypes are planned to be used in flight testing, to aid in a smooth certification process of the aircraft.

4. Design Iteration Tools

Because of HyBird's unconventional design and the increased complexity of its hybrid propulsion system, it exceeds the scope of the conventional equations in classic aircraft design such as presented in Roskam [59]. Therefore, a collection of digital aircraft design and evaluation tools has been developed that allows for more accurate sizing and optimization of key aircraft and mission parameters. The three main tools are a numerical mission simulation, an iterative component sizing, and mass prediction algorithm and a design space analysis and optimization tool.

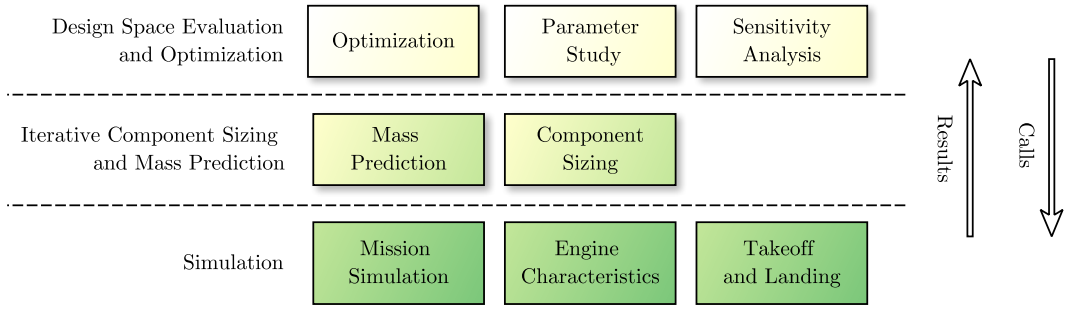

Figure 4.1.: Overview of the different tools used for design iteration

4.1. Take-Off and Landing

Typically, statistical methods are used to estimate take-off and landing distances and the required power during take-off. This approach can not provide accurate results for HyBird with its unconventional configuration and improved take-off and landing procedures. Instead, the equations of motion for take-off and landing are established and solved in order to calculate the landing distance and the required take-off power.

Sudden Loss of Thrust Compared to a conventional multi-engine aircraft, HyBird's propulsion system as shown in Figure 3.5 is more complex. Therefore, there are three major failure cases instead of only one in a conventional multi engine aircraft.

1. One wing tip propeller or electric motor has a failure. Due to this failure, the second wing tip propeller must be switched off to prevent a high yawing moment. The remaining power will be switched to the V-tail propellers.
2. Failure of one V-tail propeller or electric motor. In this case, the power would be switched to the two wing tip propellers and the remaining V-tail propeller. The resulting yawing moment can be compensated by the wing tip propellers and the vertical stabilizer.
3. Power-loss of a turbo generator. In this case the second turbo generator and the battery provide the needed power.

The three cases each pose different loads on battery and turbo generator. It is necessary that the selected battery and turbo generator are able to achieve the desired take-off distance in each case.

Take-Off Distance Take-off is split into ground roll, transition curve and climb to 35 feet. Ground roll consists of an acceleration with full thrust to the decision speed v_1 and a continued acceleration to rotation speed with reduced thrust due to OEI. Take-off is performed autonomously for cargo flights and semi-autonomously for passenger flights. Therefore pilot reaction times can be neglected during rotation. Each wheel hub motor in HyBird has $40\,kW$ of power and $300\,Nm$ of torque, and weighs approximately $8\,kg$ [43]. HyBird is capable of a steep climb after rotation of up to $10\,°$, which further reduces take-off distance. For a detailed explanation, see Appendix A.1.

Landing Distance Due to the autonomous and pilot assisting systems a steep approach and a reduced flare distance are possible. Similarly, the reaction time between touchdown and braking is reduced. Reverse thrust assists deceleration, while taking into account a sudden loss of thrust in order to satisfy 14 CFR §23.75 f) [19]. It is assumed that a propeller can provide up to $60\,\%$ of its peak thrust while in reverse [76].

To improve calculation speeds, a response surface methodology is created for the simulation tool. This surface depends on take-off mass, power loading and wing loading. For a detailed calculation with all input values, see Appendix A.1.

4.2. Mission Simulation for the Different Engine Systems

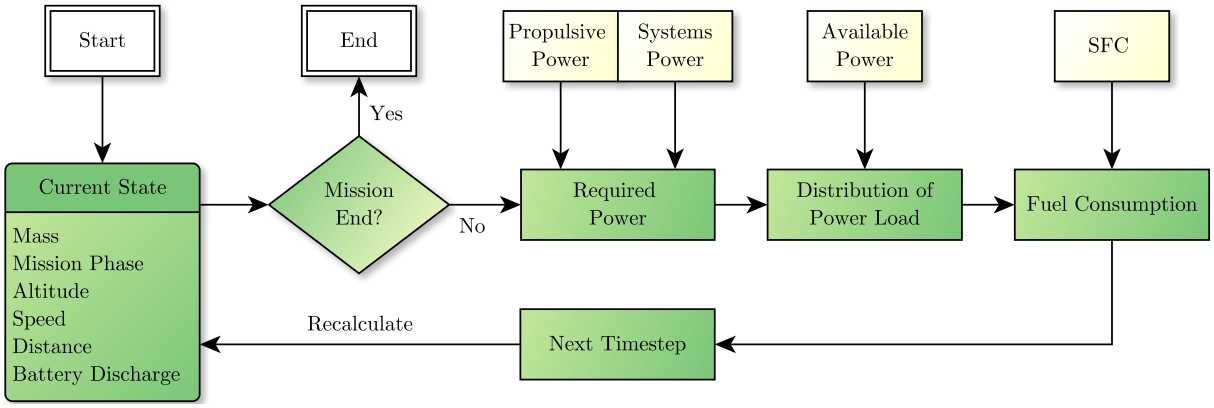

Figure 4.2.: Schematic of the mission simulation

The numerical mission simulation consists of different models that are evaluated for each mission time step. It is visually summarized in Figure 4.2. When comparing the different internal combustion engine technologies mentioned in Section 3.2.3, the critical assumption is their specific fuel consumption. The specific fuel consumption models implemented in the mission simulation are illustrated in Figure 4.3.

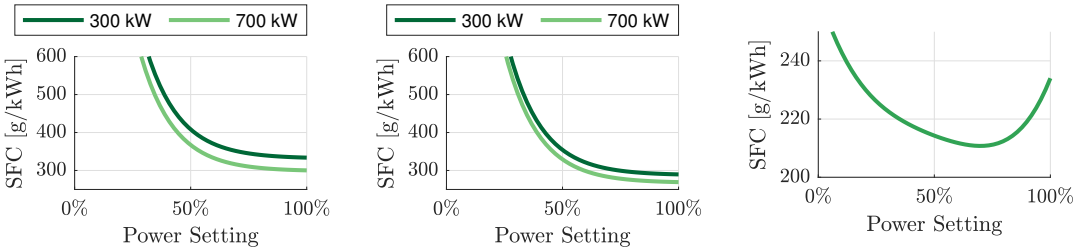

a) Turboshaft Generator [7, 22], [69, 45]

b) Recuperating Turbine Generator [70, 69, 45]

c) Diesel Generator [10]

Figure 4.3.: Specific fuel consumption models

The simulation takes into account all relevant requirements and FAA regulations such as a maximum nominal travel time of 99 minutes and a maximum speed of 250 $KIAS$ below 10,000 ft. The simulation optimizes the distribution of power load so that the engines are operated at an efficient power setting and battery usage gets minimized. As a result, taxi is performed using battery power and one engine gets switched of during cruise, if possible. Moreover, climb is performed at the best rate of climb for the available combustion engine power. A resulting altitude and power profile is shown in Figure 4.4.

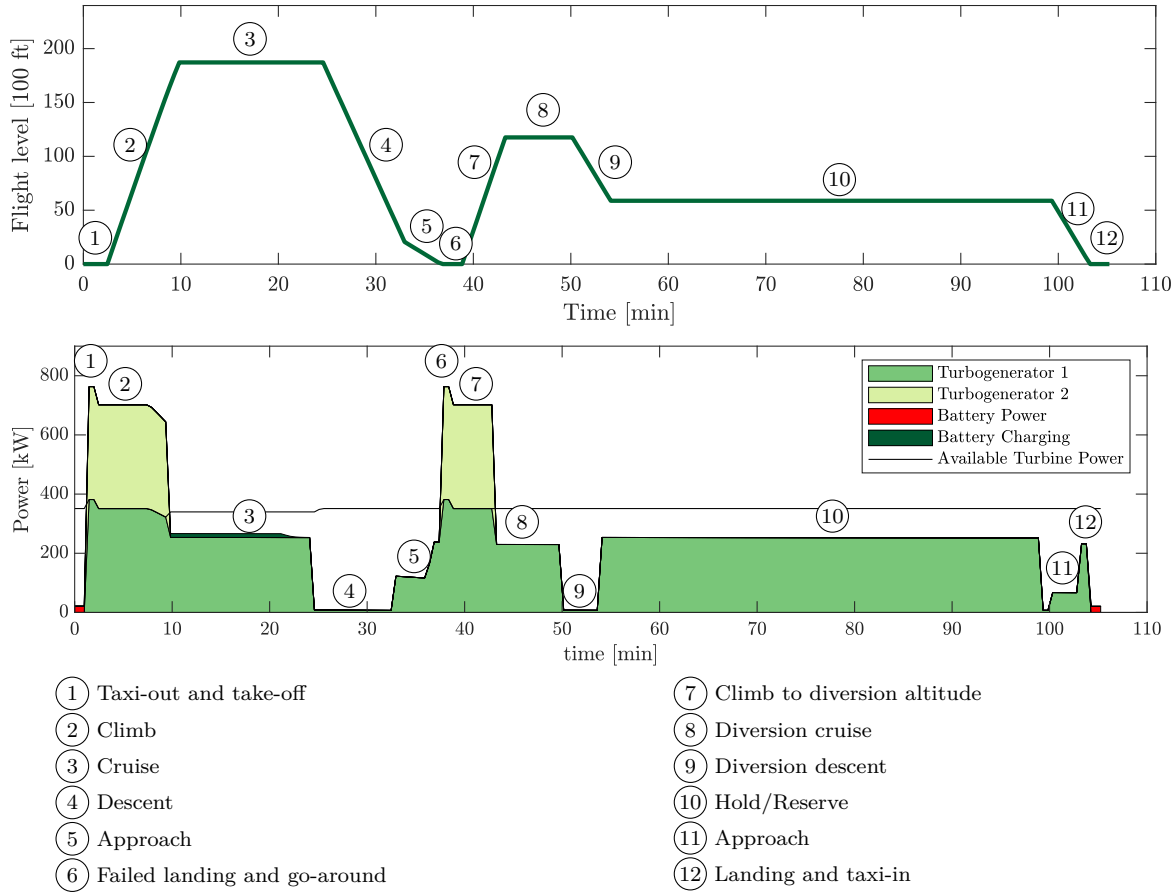

Figure 4.4.: Altitude profile and power profile of a simulated 120nm mission

4.3. Iterative Component Sizing and Mass Prediction

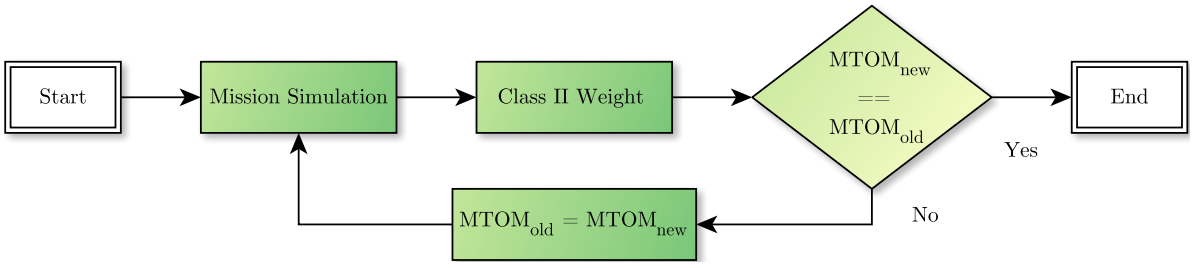

Figure 4.5.: Block Diagram of the "Mass iteration" function

This algorithm is used to size the aircraft and its components according to a given set of input parameters such as cruise speed, desired wing loading and the power-to-weight ratio of the combustion engines. It guesses a starting value for maximum take-off mass (MTOM) and executes the mission simulation with this MTOM and the other parameters as inputs. The mission simulation returns the fuel consumption and the required size of the propulsion components. These values are used to calculate a new MTOM according to the Class II method presented in Section 5.2. Inserting that calculated MTOM back into the mission simulation allows closing the loop and repeating it until both MTOMs converge.

4.4. Design Space Evaluation and Optimization

While the sizing algorithm calculates the size of various aircraft components according to a set of input parameters, the design space and evaluation and optimization tool is used to vary these parameters to optimize the aircraft or to reveal correlations between input parameters and aircraft characteristics. The most reliable and accurate approach to doing is to perform a coarse grid search to find a good starting point, followed by the application of a Nelder-Mead algorithm [48]. The design space consists of parameters such as cruise speed, wing loading, power-to-weight ratio and cruise altitude. The optimization algorithm can minimize or maximize one specific parameter. For HyBird, a metric called energy cost is chosen, which was introduced by Stoll [70]. It is the sum of the fuel cost, battery depreciation and electricity costs per nautical mile. The fuel cost is assumed to be \$3.50/gallon [70], which is about twice the current fuel price [4]. However, using carbon-neutral synthetic fuels or biofuels increases fuel prices significantly, which makes the price assumption reasonable. Battery costs are calculated according to [23]. There are no electricity costs because the HyBird uses excess energy during cruise flight to recharge the battery. Hence no ground charging is needed.

5. Results and Evaluation

This section presents the results of the design process described above. Describe are the power plant, the masses, take-off and landing, aerodynamics, and noise emissions.

5.1. Power Plant

The optimization results for the three evaluated combustion engine technologies are presented in Table 5.1. An optimized turbogenerator has the lowest fuel cost and battery amortization cost for all missions, and is therefore chosen as the optimum design. The central concept of this aircraft is that two propulsive engines are combined with a battery. The battery is used as a dissimilar energy in case of OEI. In the climb phase, both engines operate to reach cruise altitude quickly. In cruise, one engine can be switched off. HyBird can perform every mandatory operation, in case of OEI, with just one turbine. Therefore redundancy can be achieved, see Section 4.1. Through the high yaw moment, in case of a failure of a wing-tip propeller, the sizing of the electric motors is different. As a result, the power of the propeller at the V-tail is twice that, the wing-tip propellers. Therefore, each V-tail propeller has a nominal power of $200\,kW$, and each wing-tip propeller has a nominal power of $100\,kW$. In case of a propeller power-train failure, the remaining ones can compensate for that loss in power by shortly exceeding their, see Section 4.1.

	Turbogenerator	Turboshaft	Turbodiesel
$MTOM$ $[kg]$	3782	3751	4651
$P_{singleengine}$ $[kW]$	382	380	399
$P_{Battery}$ $[kW]$	183	179	381
$m_{singleengine}$ $[kg]$	109	87	398
$m_{Battery}$ $[kg]$	61	60	127
Fuel per Passenger 100 km (380 nm) $[kg/100km]$	2.0	2.2	2.3
Fuel per Passenger 100 km (120 nm) $[kg/100km]$	2.8	3.0	2.8
Fuel Costs $[\$/nm]$ (380 nm)	0.38	0.42	0.44
Fuel Costs $[\$/nm]$ (120 nm)	0.54	0.57	0.55
Battery Amortization Costs$[\$/nm]$ (380 nm)	0.005	0.005	0.03
Battery Amortization Costs$[\$/nm]$ (120 nm)	0.016	0.015	0.084
Energy Costs $[\$/nm]$ (380 nm)	0.39	0.43	0.47
Energy Costs $[\$/nm]$ (120 nm)	0.56	0.59	0.63

Table 5.1.: Result of optimization for three different power plants; turbogenerator, turboshaft and turbodiesel; the cheapest power-plant is the turbogenerator with energy costs of 120 nm mission for 0.56 \$/nm

Propeller Sizing

The propellers diameters are designed according to Method A of Torenbeek [75] resulting in a diameter of 3 m. To take noise into account and find the rotational speed of the propellers, Method B of Torenbeek [75] is applied. For low noise emissions, a tip Mach-number of 0.4 during take-off is chosen [63]. Lastly, the propellers are evaluated through the performance diagram of Torenbeek [75]. Table 5.2 shows all the results from those equations. It also proves that three blade propellers are feasible.

Flight Phase	Altitude h $[ft]$	M $[-]$	M_{tip} $[-]$	n $[1/min]$	J $[-]$	C_p $[-]$	η_P $[-]$
Take-Off	35	0.1	0.4	839	0.83	0.24	0.70
Climb	1,150	0.15	0.4	800	1.25	0.29	0.75
Climb	10,000	0.25	0.5	905	1.81	0.26	0.89
Cruise	27,000	0.43	0.67	1025	2.5	0.12	0.85

Table 5.2.: Propeller sizing in take-off, climb and cruise; climb in an altitude of 1,150 ft is the overflight over the noise measurement 2,500 m after take-off

5.2. Mass Breakdown and Center of Gravity

To find the accurate weight of the airplane, two methods are applied. The first method applied is based on mass fractions. This paragraph will solely focus on finding the weight as apposed to the simulation. The second method is based on statistics for single components, using Roskam [61]. Since this allows for the calculation of the components weights, the center of gravity (CG) is found in the process.

The second method is called Class II Method for Estimating Airplane Component Weight [61]. It is divided into three main weight groups: the structural weight, the weight of the power plant and the fixed equipment weight. Calculations are executed according to the steps provided by Roskam. However, due to the proven formulas provided this section will only examine the modified equations in detail.
The structural weight is calculated using the USAF method. By selecting this method instead of Torenbeek, it can be assured that the calculations are done with the boundaries of said method. To reduce weight, and thereby assure a short runway length the aircraft is build form a carbon sandwich structure. In Kehrle and Kolax [34] reductions of up to 28 % are made from switching from a metal hull to a sandwich body. However, to take lightning strikes into account, Klett [36] suggests limiting using a maximum reduction in weight to 25 %. This was subtracted from every structural component. Moreover, the V-tail is accounted for by super positioning the horizontal and vertical empennage. For the power plant mass, the weights were calculated using the specific power of various parts, as shown below in combination with the required:

- Specific power of the recuperating turbine generator is set at 3.4 kW/kg [70]
- The power density of the e-motors and generator is chosen to be 15 kW/kg [43]
- Inverter and rectifier have a power density of 62 kW/kg [25]
- The specific power cable mass is estimated to be about 40 kW/kg [12]
- Propeller weight is set at 50 kg per propeller, [70]
- Battery: specific power of 3000 W/kg and specific energy of 65 Wh/kg [25]

The subsystems for the power-plant are calculated using the method of Torenbeek [75]. The Torenbeek method is applied because those methods best fit our application for power plant weight estimation. For the fixed equipment, applying the Cessna method [61] provides most reasonable values. In addition to the standard equipment the calculations for the system weight of Coanda flap system is added with a Mass of 60 kg, see Section 5.4.2. In Table 5.1 are the masses for the power-train, structure and fixed equipment shown. This results to an empty mass of 2568 kg.

Component	Mass	Amount	Mass Total
Turbine	109	2	218
Battery	61	1	61
E-Motor Front	27	2	54
E-Motor Back	13	2	26
Generator	25	2	50
Engine Control	11	2	22
Engine Start	1	2	2
Inverter Front	24	2	48
Inverter Back	12	2	24
Rectifier	23	2	46
Power cable	23	1	23
Propeller	50	4	200
Fuel System	150	1	150
Power-Train			**924**

Component	Mass	Amount	Mass Total
Wing	122	1	122
Empenage	27	1	27
Fuselage	1065	1	1065
Gear	24	1	24
Structure			**1238**

Component	Mass	Amount	Mass Total
Flight Control	70	1	70
Oxygen System	17	1	17
Furnisching Weight	163	1	163
Paint	11	1	11
Coanda	75	1	75
Avioncis	70	1	70
Fixed Equipment			**406**

Figure 5.1.: Power-Train, Fixed equipment and Structure component mass results in kilogram

5.3. Take-Off and Landing Distances

With the resulting values of the simulation, the program MATLAB is used to calculate the take-off and landing performance with all input values. For this purpose the calculation is carried out using the differetial equations as described in Section 4.1 and Appendix A.1. For the OEI case with wing tip propeller failure, there is a pitch moment generated by the V-tail propeller. Therefore, the take-off is executed with $10\,^{\circ}$ trim downwards of the V-tail to lower the moment. Details can be found in Section A.5. Table 5.3 displays the distances for the three cases of OEI. They are calculated with the maximum take-off weight (MTOW) in standard atmosphere at sea level, and for high altitude airports at 10,000 ft. Those conditions are in accordance to 14 CFR §23.2105 a), respectively b) [19].

Failure	WTP-PT	VTP-PT	TG	AEO
Take-Off Distance l_{TOD} $[ft]$	682 (936)	670 (903)	683 (939)	660 (875)
Landing Distance l_{LD} $[ft]$	691 (847)	680 (833)	692 (848)	670 (820)

Table 5.3.: Take-off distances over 35 feet with OEI - Comparison between different failures; Without brackets at standard atmosphere and with brackets in an height of 10,000 ft; WTP-PT: wing-tip propeller power-train; VTP-PT: wing-tip propeller power-train; TG: turbogenerator

For conclusion, all failures have almost the same influence on the take-off and landing distance. The acceleration stop distance for all faults is 585 ft. The requirements are met in both airport altitudes as shown in Table 5.3.

5.4. Aerodynamics

This section presents the aerodynamic design which includes the lift distribution of the wing, the design of the high-lift system with a Conada flap and the empannage. The control surfaces are designed according to Roskam [60], to ensure sufficient pitch, yaw and roll authority during all flight conditions.

5.4.1. Lift Distribution and Twist

The reference wing area results from the design chart described in Section 3.3 and the MTOM to a value of $S_{ref} = 15.4\,m^2$. The Davis Basic B-24 airfoil with a low drag coefficient at the design Mach and Reynolds number is selected [9, 17]. With a relative thickness of 16 % it is also possible to install the Coanda system into the wing.
The lift distribution is designed with the Prandtl lifting-line theory. To reach maximum efficiency in cruise configuration and reduce induced drag, by twisting the wing, an elliptical circulation distribution is accomplished. The design lift coefficient is $C_L = 0.5$. The taper ratio is chosen to increase the maximum lift coefficient of the whole wing at take-off and landing. The detailed distribution of twist, circulation and lift are illustraed in Appendix A.2 in Table A.1. Table 5.4 resulting geometric parameters of the wing. The zero-lift drag coefficient of the aircraft $C_{D,0}$ is estimated by the Class II Method by Gundmundsson [29] to $C_{D,0} = 0.019$, details in Appendix A.3.

Properties	Value
Wing Area S_{ref}	$15.4\,m^2$
Span b	$14.15\,m$
Aspect Ratio A	13
Taper Ratio λ	0.7
Glide ratio L/D	22

Table 5.4.: Geometric parameter of the wing

5.4.2. Coanda High-Lift System

To reach a short take-off and landing distance extremely high lift coefficients are needed and therefore a Coanda flap design with a droop-nose is chosen. One advantage over modern fowler flaps and slats is that they emit less noise. This is due to the fact that they have no sharp edges. Furthermore, the droop-nose reduces unstable flow structures on the upper side of the wing, which leads to the higher efficiency of the Coanda flap. One disadvantage of the flaps are the required electrical power, and the weight for the compressor, which is discussed later.

This active high-lift system is shown in Figure 5.2. At the upper surface of the airfoil, a thin jet is blown over the highly angled flap. Due to the Coanda effect, the air can follow the deflection of 65 ° downward, generating lift in the process [52]. The needed air for the jet is sucked in by a compact electric compressor, which is integrated into the wing (see Figure 5.2 and 5.3) at 61 % chord length as investigated by Burnazzi [14]. The suction effect reduces the boundary layer of the suction side upstream of the blowing slot significantly, which increases the efficiency of the Coanda effect, as a lower jet momentum is needed.

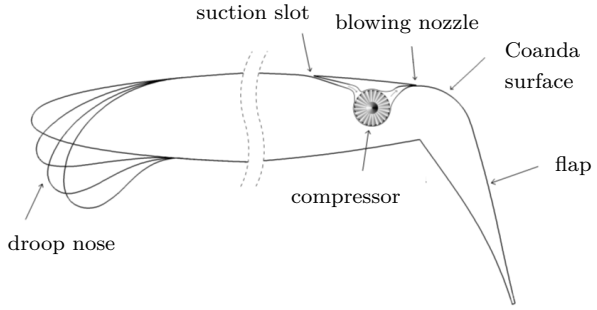

Figure 5.2.: Airfoil with droop nose, integrated compressor and Coanda flap [14]

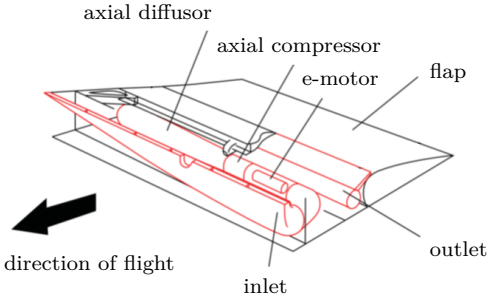

Figure 5.3.: Integration of the compact electrical compressor in the wing [67]

The jet height and mass flow are optimized for high lift coefficients and a low required power according to Burnazzi [14]. By combining the Coanda flap and droop-nose a $C_{l_{max}} = 6.0$ is achieved. To sustain this lift coefficient at take-off speed a mass flow of $4.6\,\frac{kg}{s}$ and an electrical power of $47.4\,kW$ are required. For details about the power calculation see Appendix A.4. For redundancy there are three compressors, as described by Seume [67], in each wing with a power of $12\,kW$ and a mass flow rate of $1.2\,kg$. With this configuration the failure of one compressor can be compensated by the other two. The weight of all six compressors and the six electrical motors results to $75\,kg$ according Teichel, [74].

In order to optimize $C_{L,max}$, the Coanda flap is sized as large as possible and it spreads over 77 % of the wing span. Thus it neither interferes with the wing tip propellers or the fuselage. ΔC_L and $\Delta C_{L,max}$ are calculated according to [62], as well as the maximum drag coefficient.

In addition to that, the extreme high lift coefficient generates a high induced drag with $C_{D,ind} = 0.42$, which has to be considered for the take-off calculations. The moment coefficient of the Coanda flap C_m, 2d airfoil, and of the 3d wing C_M are calculated equivalently, and all results are collected in Table 5.5.

	ΔC_l	$C_{l,max}$	$C_{d,max}$	C_m
2D flap	4.8	6.0	0.10	-2.20
3D wing	3.1	4.1	0.07	-1.4

Table 5.5.: Aerodynamics coefficients of the high lift system; lift increment ΔC_l, maximum lift coefficient and drag coefficient $C_{l,max}$ and $C_{d,max}$, moment coefficient C_m, for the two dimensional flap and the three dimensional wing

5.4.3. Empennage

The V-tail is sized in a manner that the projections of the tail are equal to a conventional configuration, according to Roskam [60]. The tail has to be high enough that the propellers, which are mounted at the tip of the V-tail, are not in the downwash of the wing. This is done in order to minimize noise. The projected span has to be $b_h > 3.5m$ to have sufficient space between the propellers. Furthermore, it has to be large enough to compensate for the pitch moment generated by the propellers during take-off, as described in the next paragraph and Appendix A.5. As a result, HyBird's volume coefficient for the horizontal part $\overline{V_h}$ is larger than comparable aircraft, which typically have a volume coefficient of about 0.9. The cord length is set to $c_h = c_v = 0.89m$ with a taper ratio of $\lambda = 0.8$. All dimensions of the V-tail are shown in Table 5.6. The angle between the tail and the horizontal line results to $\Gamma = \arctan(\frac{S_v}{S_h}) = 38°$.

Empennage	$x\,[m]$	$\overline{V}\,[-]$	$S\,[m^2]$	$c\,[m]$	$b\,[m]$
horizontal	6.63	1.62	4.13	0.89	4.66
vertical	6.63	0.10	3.22	0.89	3.64

Table 5.6.: Dimensions of an equivalent conventional tail, lever of the tail unit x, volume coefficient $\overline{V}$, area S, cord length c and projected span b

The control surface is sized over a length of 85% of the span and 35% of the chord length. This ensures that there is enough space at the root at full rudder deflection and for the casing of the electric motor at the tip. As an airfoil, the NACA0012 with a plain flap is used. With an angle of attack of $\alpha = 10°$ a lift coefficient of $C_l = 1.0$ is reached. At take-off, a lift coefficient of the tail of $C_{l,TO} = -1.3$ is required to compensate the pitch torque of the propeller (see Appendix A.5). This takes the increase of stagnation pressure by the propellers with a factor of 1.1 into account. According to Roskam [63], a maximum lift coefficient of the tail unit is calculated to $C_{L,max,tail} = \pm 1.9$ at an flap angle of $\delta_{tail} = 35°$. Goett [27] proved even higher lift coefficients for a plain flap up to $C_l = 2.2$ with $\alpha = 18°$ and $\delta_{tail} = 60°$. Therefore, enough controllability of pitch is guaranteed. The controllability of yaw is insignificant because of the large volume coefficient.

5.5. Noise Emissions

The procedure during the measurement of the noise level is described in 14 CFR Part 36 Appendix G [20], and consists of take-off (first segment) and climb (second segment). The take-off noise level measurement is negligible because of the considerable distance to the microphone. Therefore, the flyover in climb configuration is critical for the measurement. In the climb configuration, the noise generated by the turbine, including the exhaust, as well as the general aerodynamic noise, is more than 10 dB lower than the noise level of the propellers [63]. Therefore, only the propeller generated noise is considered. The calculation of the propeller noise is conducted according to Roskam [63]. The rotational Mach number at the tip of the propeller equals 0.4 to reduce noise, as described in Section 5.1. The A-weighted noise is calculated by adding up all partial noise levels, as illustrated in Table 5.7. The result is a maximum noise emission of 64 dB. For comparison, a normal conversation and a TV speaker have a level of 65 dB; a washing machine in the spin cycle has a level of 75 dB [5].

Partial Noise Level	Value
Single Propeller Noise (P_{prop}, $M_{rot,tip}$)	70 dB
Correction Far Field (n_{blades}, d_{prop})	4 dB
Correction Atmospheric Absorbtion ($h = 1150\,ft$)	-7 dB
Correction Azimut Angle	1 dB
Correction 4 propeller	6 dB
Correction Precived Noise Level (d_{prop}, M_{helix})	4 dB
Correction "A Weighted" Noise	-14 dB
"A Weighted" Noise	dB(A) = 64 dB

Table 5.7.: "A Weighted" Noise Level dB(A) during overflight in climb; altitude to measurement 1,150 ft

6. Operational Concept

This section first describes the operation of the airplane when no pilot is onbaord. Then it illustrates a typical operation day of HyBird.

6.1. Autonomous Operations

In autonomous flight mode, other aircraft and the air traffic control must know the status of HyBird. Therefore, it sends out a transmitter signal, with important flight information. If the airplane deviates from the standard procedures, a ground-based pilot interferes and controls the airplane. This is necessary to ensure safety. The aircraft is equipped with health monitoring sensors, ensureing the functionality of all critical systems and components.

For airports without any ground-based facilities, the aircraft has to rely solely on onboard systems. In that case, the HyBird follows a strict procedure that is entirely independent. The take-off procedure for fully autonomous flight is executed according to the following steps:

1. If all passengers and/or cargo are loaded, HyBird computer checks the signals in the seats to verify that all people are seated and buckled up. If that's the case, the door is closed. Force sensors in the landing gear are used to check if the aircraft's mass and center of gravity are within the required bounds.
2. During taxi the aircraft uses all sensors, see 3.5.2, to check the surrounding for obstacles. If a passenger decides to unbuckle himself, the aircraft will stop immediately at a safe position.
3. Once on the runway, the HyBird stops and uses the front LIDAR and radar to check the runway, followed by initiating take-off if there are no hazards.

For the landing the steps below are executed:

1. Check the runway with the front LIDAR and radar sensors.
2. If the runway is clear, the aircraft attempts to land. In case of a failed attempt, it makes a go-around and retries once more. Is there a second failed approach, the aircraft initiated contact with ground-based pilot who can assist with the landing.
3. After a successful landing, the plane informs the base of its status.

At a large airport, with an abundance of aircraft taking off and landing, timing is essential. The tower coordinates take-off and landing. In this case, HyBird can follow voice commands according to the standard air traffic radio communication protocol. A deterministic, pre-programmed system identify the voice recognition, which identify the necessary sequences for HyBirds autonomous system. If there is a external interference and HyBird can not follow the voice commands a ground-based pilot takes over the control.

6.2. Mission Plan

A standard operating day is defined in the design specifications of NASA and DLR [1].The plane is operated 300 days a year for 18 hours a. It is split into two segments. Firstly, a twelve-hour long segment of flying passenger missions. Secondly, a six-hour long segment of executing cargo missions. The following is assumed for mission planning:

- The aircraft is operating out of one airport, resulting in an even number of flights per segment
- The standard mission is 120 nm, with a gate to gate time of 38 min.
- The turn around time is 45 min for passenger mission and 30 min for the cargo mission
- Switching between passenger configuration and cargo configuration takes 60 min.

Figure 6.1 illustrates a standard operating day. It not only includes aircraft usage but also when pilots are needed. This results in eight possible passenger flights and four possible cargo flights per day. As the figure shows, this already includes the switch from passenger to cargo and back.

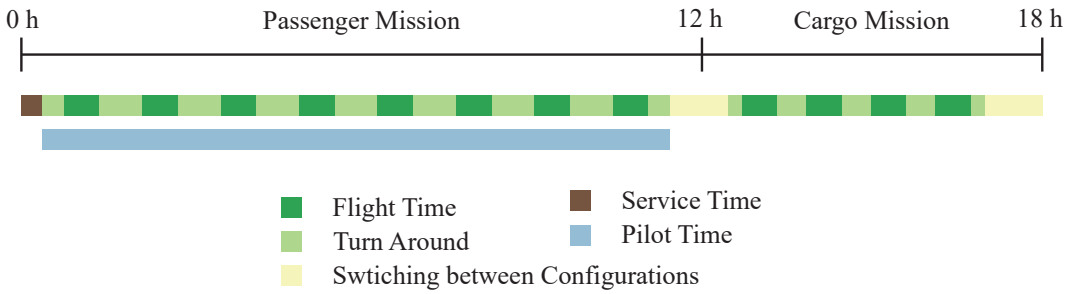

Figure 6.1.: Mission Plan for a Standard Operating Day

The amount of time the plane spends in passenger configuration is equal to the amount of time pilots are needed, which is 11.1 h per day. Calculating the time spent in cargo configuration leads to the amount of 4.6 h per day. When taking the switching from cargo to passenger configuration into account, the total usage time is 17.7 h per day. The result is that the plane is only unused for 22 minutes of the day, which can be used for small service activities such as cleaning.

7. Cost Analysis

To calculate the purchase costs of HyBird, the estimation method described in Gudmundsson [29] is applied. The prices of the method are adjusted to the dollar prices of January 2018 [13] and follwing properties are selected:

- Production rate is set to 8.33 airplanes per month, which equals to 800 planes over eight years
- The Coanda flap system is evaluated as a complex flap system because of the needed tubing and installment of the compressors
- The complete airframe is a carbon fiber structure
- Certification of the airplane is assumed to be under FAR Part 23
- The rate for engineering, tooling, and manufacturing are set to 98.1 $\$/hr$, 54.5 $\$/hr$, and 43.6 $\$/hr$ respectively. [29]
- The quantity discount factor (QDF) is calculated using an experience effectiveness factor of 80 % [29]

By applying all these assumptions, the estimated purchase price is calculated to be $2,430,000. With the price known, it is possible to calculate the cost per nautical mile. Two calculations are performed to illustrate the cost for a standard mission of 120 nm as well as the cost for the maximum range of 380 nm. However, the reason for selecting the 380 nm mission is to illustrate the cost for the maximum operating range. To show the cost of the airplane independently of the utilization, this section examines the cost per nm. In the overview of fulfilled requirements, the value per nm per passenger are described in Table 8.2, assuming full utilization. Using the mission plan according to Section 6.2 is the bases of the cost calculations. The mission overview in detail, as well as aircraft specific values, can be found in Table 7.1.

	120 nm Mission			380 nm Mission		
	HyBird	402C	PC-12	HyBird	402C	PC-12
Flight time [min]	38	48	38	99	126	99
Passenger flights per day	8	6	8	4	4	4
Cargo flights per day	4	4	4	2	2	2
Flight hours per year [hr]	2,280	2,400	2,280	2,970	3,780	2,970
Pilot time per day [hr]	11.1	9.3	11.1	9.6	11.4	9.6
Time between overhaul [hr]	6,000*	2,700*	3,500*	6,000*	2,700*	3,500*
Price overhaul [$/kW]	560*	160*	520*	560*	160*	520*
MTOM [lb]	8,320	7,210*	10,450$^{\triangle}$	8,320	7,210*	10,450$^{\triangle}$
Purchase price [k$]	2,430	550*	4,700*	2,430	550*	4,700*

Table 7.1.: Missions overview of the HyBird, the Pilatus PC-12 and the Cessna 402C, $^{\triangle}$[53], *[70]

For comparison, the Pilatus PC-12 and the Cessna C402 are selected and examined under the same conditions. The general assumptions for the different cost calculations are:

- Maintenance: Is set to $147 per flight hour for the PC-12, [70], $243.6 per flight hour for the C402 [5] and is calculated according to Gudmundsson, [29]
- Insurance: The yearly insurance payments are calculated according to [70] , making it $1.68 per million purchase price plus $3.36 per flight hour.
- Landing fee: Is assumed to be $4.2/1000 lb, [70], in 2016
- Overhaul: It differs depending on the aircraft, the values can be found in Table 7.1
- Pilot cost: $42 / hr, [70]
- Interest: The aircraft is paid off over seven years with an interest rate of 6.5%
- Fuel: The fuel consumption per year is calculated during the mission simulation as described above with a price of 3.68 $/gallon, [70]

The result for the standard 120 nm mission is shown in Figure 7.1. It displays the different categories mentioned above. Comparing these, three things become very evident. First, the HyBird is the cheapest to maintain and has the lowest fuel costs. The reason for this is the unique feature of always running the turbine at optimum efficiency. This is combined with a low drag coefficient, thereby lowering fuel consumption further. Having the low maintenance cost originates from having 6000 hours between overhauls, as well as, having one turbine only run at cruise. However, the 402C has low-interest cost and overhaul cost. The origin behind the low-interest cost is the low purchase price of $550k, and the overhaul cost for the simple engine. The total cost per nautical mile can be summed up to $5.59 for the PC-12, $3.70 for the 402C and $3.46 for the HyBird. However, the interest rate only applies the first seven years, because it is assumed the aircraft is paid for in full after that, reducing the cost further. This leads to the following total cost per nautical mile: $3.61 for the PC-12, $3.42 for the C402 and $2.43 for the HyBird.

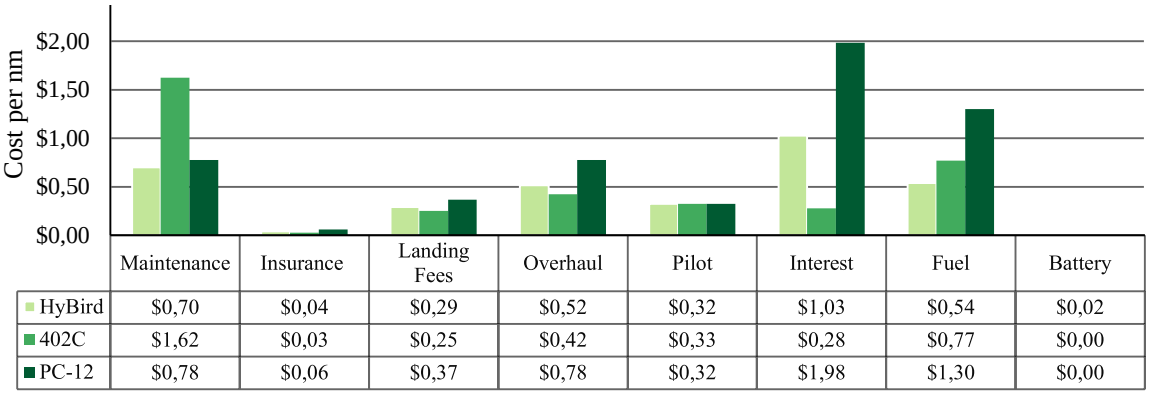

	Maintenance	Insurance	Landing Fees	Overhaul	Pilot	Interest	Fuel	Battery
HyBird	$0,70	$0,04	$0,29	$0,52	$0,32	$1,03	$0,54	$0,02
402C	$1,62	$0,03	$0,25	$0,42	$0,33	$0,28	$0,77	$0,00
PC-12	$0,78	$0,06	$0,37	$0,78	$0,32	$1,98	$1,30	$0,00

Figure 7.1.: Cost per Nautical Mile for a 120 nm Mission

A further illustration of that effect is shown in Figure 7.2. The figure shows the sum of the money that is saved when operating HyBird instead of the PC-12 or the 402C. When the interest is paid off after seven years, the cost decreases, which becomes apparent around the three million miles mark.

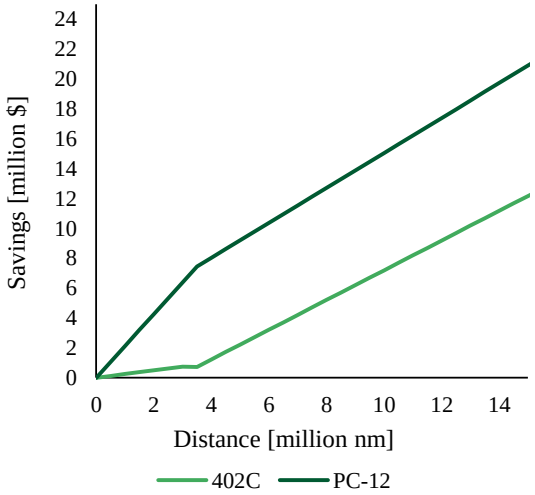

Figure 7.2.: Saved operating costs when using HyBird instead of PC-12 and 402C respectively

For the 380 nm mission, the data presents a similar picture in terms of accumulated cost. It is important to note that the 402C can fly the 380 nm only at 180 $KTAS$, resulting in a flight time of 126 min. Therefore, the 402C needs to be viewed with caution in this mission. As for the full cost of the mission, there are a few noticeable points. First, HyBird has a lower fuel cost per nautical mile for the 380 nm mission than for the 120 nm mission. This is due to the more extended cruise period, thereby spending more time with only one turbine running at optimum efficiency. Second, the landing fees are lower due to less flights as shown in Table 7.1. Third, the interest rate is also lower due to more time the plane spends in the air. Forth, although the aircraft spends more time in the air, the pilot costs are lower because the pilot only must work 9.6 hours. This all sums up to the following total prices: The PC-12 costs $4.57 per nm, the 402C costs $2.92 per nm, and the HyBird costs $2.31 per nm. If the assumption is made, that the interest is paid off the prices further decrease: The PC-12 then costs $3.32 per nm, the 402C costs $2.77 per nm and the HyBird costs $1.66 per nm.

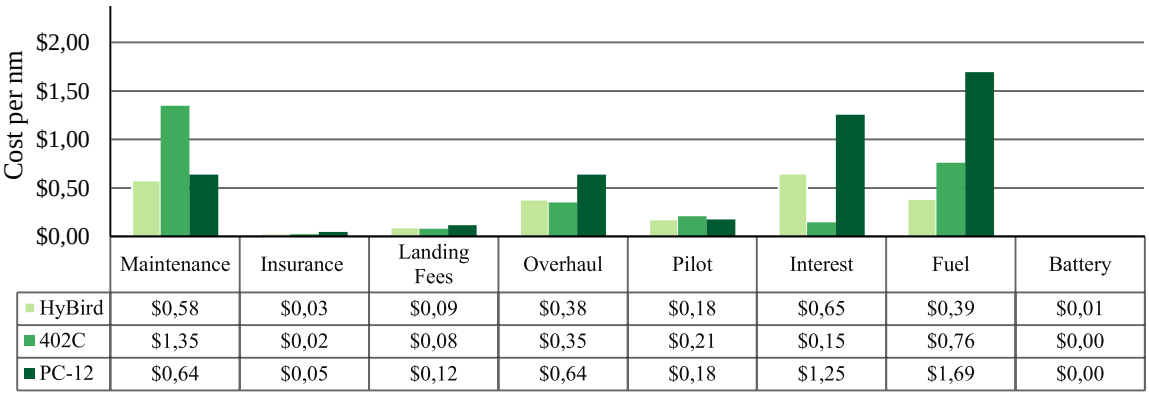

	Maintenance	Insurance	Landing Fees	Overhaul	Pilot	Interest	Fuel	Battery
HyBird	$0,58	$0,03	$0,09	$0,38	$0,18	$0,65	$0,39	$0,01
402C	$1,35	$0,02	$0,08	$0,35	$0,21	$0,15	$0,76	$0,00
PC-12	$0,64	$0,05	$0,12	$0,64	$0,18	$1,25	$1,69	$0,00

Figure 7.3.: Cost per Nautical Mile for a 380 nm Mission

Comparing the two missions, it becomes apparent that the HyBird costs 8.7% less than one of the most common used commuter aircraft on a common commuter mission. It also costs 38.5% less than an executive propeller aircraft. For the extended 380 nm mission, that gap increases to 21.2% and 49.6% respectively.

8. Concept Summary

The following chapter summarizes the most important characteristics of Hybird.

8.1. Key Technologies and Synergies

Positioning of the Propellers at Wing Tip and V-Tail The effective area of the propeller is much larger if they are placed at the wing tip and on the V-tail compared to at the nose or in front of an engine nacelle. Moreover, there is an undisturbed incident flow which leads to decreased propeller noise. The high wing design allows a large propeller diameter, which reduces propeller speed and noise. With four propellers instead of three or two, a failure during take-off can be better handled. The wing tip mounted propeller especially reduces the induced drag, which leads to a high efficiency at cruise. Furthermore, the force on the root of the wing is decreased.

Coanda High Lift System The coanda flaps generate a very high lift coefficient of $C_L = 4.1$ at take-of. This allows to significantly increase the wing loading while maintaining a short take-off field length. As a consequence of the decreased wing size, parasitic drag during cruise is reduced. The electric energy required for the compressors is available anyway because of the electric propulsion system. Furthermore, the flaps have less noise emissions compared to fowler flaps.

Two Turbines and Generators in the Nose With two turbines in the front one of them can be switched off at cruise with the other running at its optimum operating point. With the engine placement in the fuselage no additional drag is generated. Furthermore, this placement is beneficial for the generated noise level.

Wheel Hub Motors The important benefit of the wheel hub motors is that a quiet and safe taxi is possible without running propellers. Additionally they provide further acceleration at take-off.

Fast Convertible Cabin The cabin is designed for passenger as well as cargo operation with no compromises. A fast conversion from passenger to cargo and the other way around guarantees a high utilization of the aircraft.

Fly-By-Wire and electric aircraft systems Fly-By-Wire reduces aircraft weight and increases safety. Electric actuators and electric cabin pressurization and air conditioning reduce weight and maintenance.

Autonomous Flight HyBird can be autonomously operated on cargo missions. The installed systems also assist the pilot during passenger flights. This reduces pilot workload and allows to reduce the take-off and landing distances.

Carbon Fiber Composite Structure A carbon fiber composite structure significantly reduces structural weight and therefore fuel consumption and operating costs.

Sustainable Fuels While using alternative synthetic fuels or biofuels increases operating costs, it allows the carbon-neutral operation of HyBird. This is an important contribution to achieving the goal of a carbon-neutral growth of the aviation market from 2020 onwards [2].

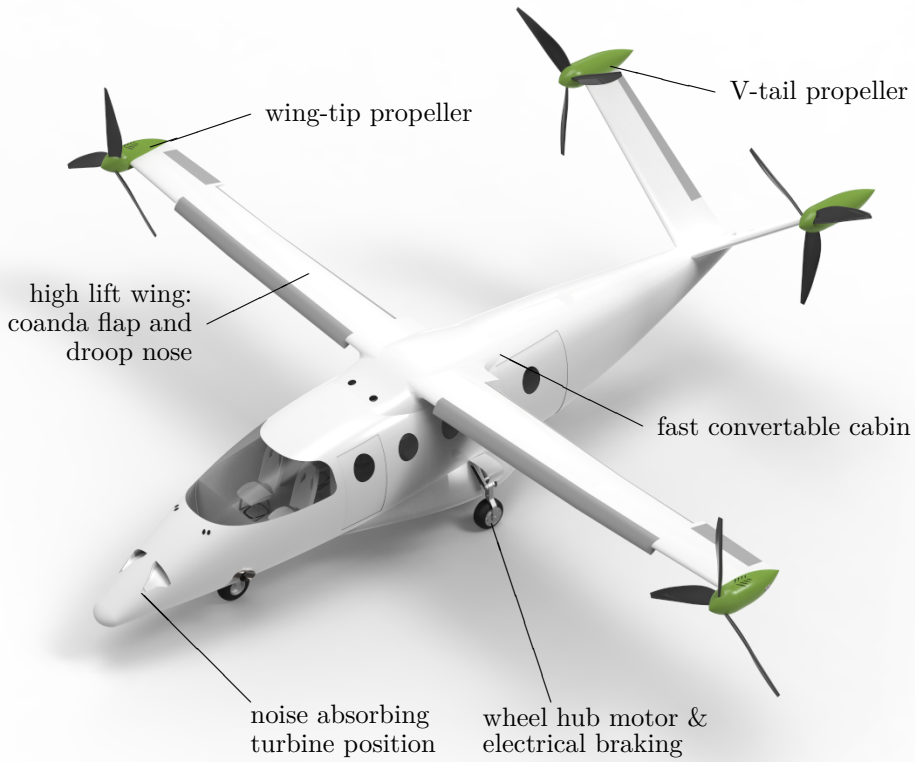

Figure 8.1.: Overview for HyBird with Key Technologies

8.1.1. Feasibility & Technology Readiness Level

In this section, the key technologies for HyBird are summarized and evaluated according to their Technology Readiness Level (TRL), [47]. All components, which have a TRL equal to or greater than 5, have the potential to be flight-proven by 2025, [6]. Since all key technologies fulfill this criterion, it is assumed that successful entry into service of HyBird in 2025 is feasible.

Component	TRL	Source
Autonomous System	6	[54]
Battery	5	[47]
Coanda System	5	[47]
Electric Motor	5	[47]
Recuperating Turbine Generator	5	[70]
Sandwich structure	7	[47]
V-Tail Propeller	7	[24, 47]
Wing-Tip Propeller	5	[47]
Wheel Hub Motor & Electrical Braking	7	[40, 47]

Table 8.1.: Key Technologies with Technology Readiness Level

8.2. Overview - Top Level Aircraft Requirements

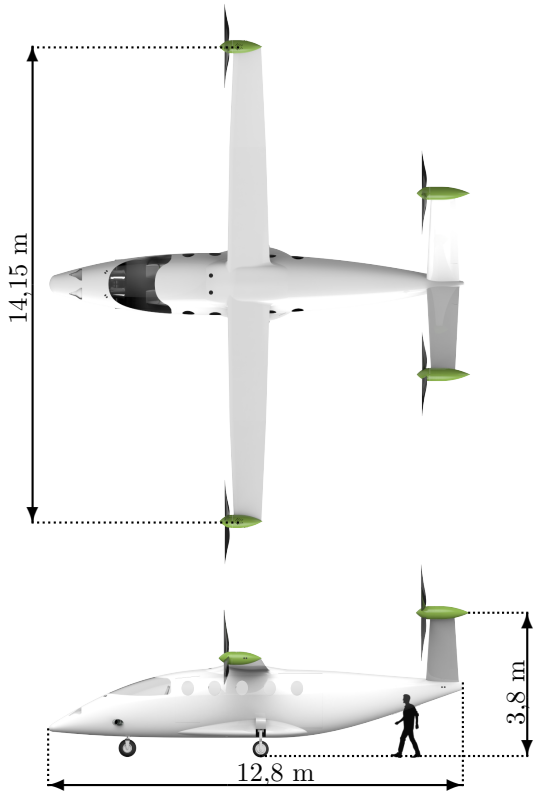

Propeller Diameter 3 m

Performance

The HyBird has the following performance under international standard atmospheric (ISA, sea level) conditions:

Take-Off distance over 35 ft obstacle (MTOM)	683 ft
Landing distance over 35 ft obstacle (MLM)	693 ft
Rate of climb at 10,000 ft altitude (MTOM)	2500 ft/min
Nominal cruise speed	265 $KTAS$
Nominal cruise mach number	0.43
Nominal range (holding and reserves)	380 nm
Max. altitude	27,000 ft
Stall speed (MTOM)	61 $KIAS$

Masses

Max. take-off mass	3782 kg
Max. zero fuel mass	3556 kg
Empty mass	2568 kg
9 Passenger	1980 lb
Nominal payload	2000 lb
Nominal fuel	226 kg

8.3. Evaluation

In this section the aircraft design is evaluated upon its safety risks and fulfillment of the given requirements.

8.3.1. Safety/Risks and Failure Modes

The risks, challenges, and advantages in operating with a pilot are well known. For example, the human factor and imperfection are often compensated by checklists and extensive training. This leads to a concrete, trained handling in emergencies.

On the other hand, for entirely autonomous operations, there is less experience [33]. These research programs simplify the process and risks for an autonomous flight with passengers. A failure in computer systems is because of redundancy negligible. The main difficulty is in communication to the autonomous aircraft. In the case of emergencies, meaning that the deterministically programmed software is not able to solve the problem. A mayday signal is sent to a ground-based pilot, who can operate the aircraft in emergencies.

Another problem for autonomous aircraft is that during taxi and ground operations a foreign object could be encountered, leading to damage. Through the systems and without rotating propellers due to

wheel hub motors of HyBird this problem is reduced to a minimum.

Moreover, hacking is an important issue. There are various opportunities to get control over drones, [78]. For an autonomous, crewed aircraft it is also possible to hack it. Therefore, it is necessary to integrate a hacking save system.

8.3.2. Fulfillment of Requirements

In Table 8.2 are the reached requirements shown:

#	HyBird	achievement
1	9 passengers, total 1980 lb	Goal achieved
2	2000 lb of cargo	Goal achieved
3	convert from passenger to cargo within 60 min	Goal achieved
4	up to two pilots	Goal achieved
4.1	passenger operation with one pilot	Goal achieved
4.2	cargo operation without pilot	Goal achieved
4.3	in near future 4.2 at passenger operation	Goal achieved
5	380 nm range	Threshold achieved
6	reach range in less than 99 min	Goal achieved
7.1	100 nm after balked landing	Goal achieved
7.2	45 min holding at cruise speed	Goal achieved
8	683 ft TOD and 692 ft LD required	Threshold achieved
9	no leaded synthetic or bio fuel	Goal achieved
10	cabin pressure at 8000 ft	Goal achieved
11	noise level 64 $dB(A)$	Goal achieved
12.1	passenger mission according to task	Goal achieved
12.2	cargo mission according to task	Goal achieved
13	operating cost \$0.38 per mile per passenger	Threshold achieved

Table 8.2.: Overview of the achieved requirements.

9. Conclusion

The challenge of designing a modern commuter aircraft can be achieved through various configurations and methods. The configuration selected in this paper is a mix of conventional and modern approaches. Adding a V-tail results in a reduced weight. Placing two turbines inside the nose of the aircraft allows the unique configuration of a serial hybrid. This provides the HyBird with the advantage of being propelled by four larger diameter electric propellers placed at the tips of the wing and the V-tail. Thus the noise emission equals to 64 dB which is comparable to a normal conversation. Due to the position of the propeller, the induced drag is reduced. Another advantage of having a hybrid system, made from two turbines, is the possibility to shut down one engine during cruise, hence increasing the efficiency by running the turbine at an optimum power output. All those factors allow HyBird to operate at higher cruise speeds with a lower fuel consumption than its closest rival. Using the Coanda flap system enables short landing distances below 700 ft. With a range of 380 nm, the HyBird is capable of long commuter distances. Because of the installed wheel hub motors, the aircraft can taxi without any running propellers. Besides the possibility to fly in a passenger or a cargo configuration, it can operate fully autonomously. It covers 97 % of the US mainland when operating from the 20 biggest airports in the US. Since any power source can replace the turbines as generators, the HyBird plane allows staying flexible in the future as well. All those points make the HyBird a unique option for any airline because of the combination of low cost and high performance.

References

[1] Aufgabenstellung: Joint NASA / DLR Aeronautics Design Challenge 2018-2019. https://www.dlr.de/dlr/Portaldata/1/Resources/documents/2018/Aufgabenstellung_NASA___DLR_Aeronautics_Design_Challenge_2018-2019_v3.pdf. Accessed: 05.03.2019.

[2] Climate Change. https://www.iata.org/policy/environment/Pages/climate-change.aspx. Accessed: 11.03.2019.

[3] Density Population Map. https://www.census.gov/en.html. Accessed: 16.03.2019.

[4] Jet Fuel Price Monitor. https://www.iata.org/publications/economics/fuel-monitor. Accessed: 27.05.2019.

[5] Wenn aus Geräuschen Lärm wird: Dezibel-Übersicht. https://www.hoerex.de/service/presseservice/trends-fakten/wie-laut-ist-das-denn.html. Accessed: 14.06.2019.

[6] IATA: Technology Roadmap 2013. (4th Edition), June 2013.

[7] A. L. Velloci Jr. Aerospace Source Book. *Aviation Week and Space Technology*, pages 115–128, Jan. 2009.

[8] Aerofilm System. https://www.aerofilmsystems.com/en/how-it-works/. Accessed: 12.04.2019.

[9] Airfoil Tools. Davis basic b-24 wing airfoil. http://airfoiltools.com/airfoil/details?airfoil=davis-corrected-il. Accessed: 05.04.2019.

[10] R. v. Basshuysen and F. Schäfer. *Handbuch Verbrennungsmotor: Grundlagen, Komponenten, Systeme, Perspektiven*. Springer Vieweg, Wiesbanden, 2015.

[11] N. Beck, R. Radespiel, C. Lenfers, J. Friedrichs, and A. Rezaeian. Aerodynamic Effects of Propeller Slipstream on a Wing with Circulation Control by Internally Blown Flaps. *Journal of Aircraft*, 52, 2014.

[12] G. V. Brown. Efficient Flight-Weight Electric Systems, 2012.

[13] Bureau of Labor Statistics. CPI Infaltion Calculator. https://www.bls.gov/data/inflation_calculator.htm. Accessed: 19.05.2019.

[14] M. Burnazzi. *Design of Efficient High-Lift Congurations with Coanda Flaps*. PhD thesis, Technische Universität Braunschweig, 2015.

[15] Cargo Systems. https://www.cargosystems.com/. Accessed: 23.03.2019.

[16] G. Carrier and L. Gebhardt. A Joint DLR-ONERA Contribution to CFD-based Investigations of Unconventional Empennages for Future Civil Transport Aircraft. *2005 CEAS/KATnet Conference on Key Aerodynamic Technologies*, 2005.

[17] J. Dreese. Part 5: Laminar airfoils made easy. http://www.dreesecode.com/primer/airfoil5.html. Accessed: 05.03.2019.

[18] European Aviation Safety Agency. Certification Specifications for Normal, Utility, Aerobatic, and Commuter Category Aeroplanes CS-23.

[19] Federal Aviation Administration. Title 14 Code of Federal Regulations (14 CFR): Part 23 - Airworthiness Standards: Normal, Utility, Acrobatic, and Commuter Category Airplanes.

[20] Federal Aviation Administration. Title 14 Code of Federal Regulations (14 CFR): Part 36 - Noise Standards: Aircraft Type and Airworthiness Certification.

[21] C. W. Frick, W. F. Davis, L. M. Randall, and E. A. Mossmann. An Experimental Investigation of NACA Submerged-duct Entrances. *NACA ACR No. 5120*, 1945.

[22] GE Aviation. Introducing GE's Catalyst^{TM} - Advanced turboprop engine. https://www.geaviation.com/bga/engines/ge-catalyst. Accessed: 14.06.2019.

[23] I. Geiß, S. Notter, A. Strohmayer, and W. Fichter. Optimized Operation Strategies for Serial Hybrid-Electric Aircraft. In *2018 Aviation Technology, Integration, and Operations Conference*, AIAA AVIATION Forum. American Institute of Aeronautics and Astronautics, 2018.

[24] I. Geiß and R. Voit-Nitschmann. Sizing of fuel-based energy systems for electric aircraft. *Proceedings of the Institution of Mechanical Engineers, Part G: Journal of Aerospace Engineering*, 231(12):2295–2304, 2017.

[25] H. Gesell. Systembetrachtung turbo-hybrider und voll elektrischer primärer Antriebssysteme am Beispiel eines Regionalverkehrsflugzeugs: DLR-IB-AT-KP-2017-143. Master's thesis, Deutsches Zentrum für Luft- und Raumfahrttechnik, 2017.

[26] Y. Gibbs. NASA Armstrong Fact Sheet: NASA X-57 Maxwell. https://www.nasa.gov/centers/armstrong/news/FactSheets/FS-109.html. Accessed: 24.06.2019.

[27] H. J. Goett and W. K. Bullivant. Tests of NACA 0009, 0012, and 0018 airfoils in the full-scale tunnel. *NACA Report No. 647*, 1938.

[28] T. H. Grubesic and F. Wei. Evaluating the efficiency of the Essential Air Service program in the United States. *Transportation Research Part A: Policy and Practice*, 46(10):1562–1573, 2012.

[29] S. Gudmundsson. *General aviation aircraft design: Applied methods and procedures*. Butterworth-Heinemann, Oxford, UK, 1. edition edition, 2014.

[30] J. Han, D. Kim, M. Lee, and M. Sunwoo. Enhanced Road Boundary and Obstacle Detection Using a Downward-Looking LIDAR Sensor. *IEEE Transactions on Vehicular Technology*, 61(3):971–985, 2012.

[31] Y. J. Hasan, F. Sachs, and J. C. Dauer. Preliminary design study for a future unmanned cargo aircraft configuration. *CEAS Aeronautical Journal*, 9(4):571–586, 2018.

[32] P. A. Jackson, K. Munson, L. Peacock, S. Bushell, and D. Willis. *Jane's All the World's Aircraft 2011-2012*. Jane's Information Group, 2011.

[33] A. Joos. Forschungsbeitrag zur Luft- und Raumfahrttechnik. Stiftung Werner-von-Siemens-Ring, 2013. Jungwissenschaftler 2013.

[34] R. Kehrle and M. Kolax, editors. *Sandwich structures for advanced next generation fuselage concepts*, 2006.

[35] H. D. Kim. Distributed propulsion vehicles. *27th Congress of the International Council of the Aeronautical Sciences 2010, ICAS 2010*, 1:55–65, 2010.

[36] Y. Klett. Sandwich structres and their weight reduction potential. Interview, 16.05.2019. University of Stuttgart, Institute for Aircraft Design.

[37] E. Kuhn, V. Lange, and P. Zimmermann. *Paletten-Management: Leitfaden für die Praxis*. Recht & Praxis : Güterkraft. Vogel, 2005.

[38] P. L. Lasagna, K. G. Mackall, B. , and T. W. Putnam. Landing approach airframe noise measurements and analysis. *NASA Technical Paper 1602*, 1980.

[39] M. Lehmann. Flight control system and signaling to actuators. Interview, 15.05.2019. University of Stuttgart, Institute for Aircraft Systems.

[40] J. Liu, J. Yang, and Y. Xiao. Study on electric brake system of civil aircraft. In *IEEE/CSAA AUS 2016*, pages 917–922, Piscataway, NJ, 2016. IEEE.

[41] J. Loth and F. Loth. Induced drag reduction with wing tip mounted propellers. In *AIAA PAPER 84, No. (A84-2149)*, 1984.

[42] R. H. Lugg and H. Youngren. Hybrid jet/ electric vtol aircraft, 14.03.2012.

[43] Magnax bvbv. The technology: Next-gen axial flux machines. https://www.magnax.com/technology. Accessed: 18.04.2019.

[44] J.-C. Mare and J. Fu. Review on signal-by-wire and power-by-wire actuation for more electric aircraft. *Chinese Journal of Aeronautics*, (3):857–870, 2017.

[45] Modern Transport and Environment. ATR: The Optimum Choice for a Friendly Environment, 2001.

[46] M. D. Moore. Distributed Electric Propulsion (DEP) Aircraft. NASA Langley Research Center, 2012.

[47] NASA. Technology readiness level definitions. https://www.nasa.gov/pdf/458490main_TRL_Definitions.pdf. Accessed: 24.05.2019.

[48] J. A. Nelder and R. Mead. A Simplex Method for Function Minimization. *The Computer Journal*, 7(4):308–313, 1965.

[49] J. Patterson and G. Bartlett. *Effect of a Wing-Tip Mounted Pusher Turboprop on the Aerodynamic Characteristics of a Semi -Span Wing.* AIAA PAPER 85-1286, No. (A85-39700), 1985.

[50] J. Patterson and S. G. Flechner. Exploratory wind-tunnel investigation of a wingtip-mounted vortex turbine for vortex energy recovery. *NASA Technical Paper 2468*, 1985.

[51] M. Pfeiffer. Neue Dornier 228 für NCA. *Flugrevue*, 07.2019.

[52] K. C. Pfingsten, R. D. Cecora, and R. Radespiel, editors. *An experimental investigation of a gapless high-lift system using circulation control*, 2009.

[53] Pilatus Aircraft Ltd. PC-12NG Just The Facts, 2013. Switzerland.

[54] F. Pinchetti. Required systems and sensors for autonomous take-off and landing. Interview, 24.05.2019. University of Stuttgart, Flight Mechanics and Control.

[55] F. Pinchetti, J. Stephan, A. Joos, and W. Fichter. Flysmart - automatic take-off and landing of an easa cs-23 aircraft. In *Deutscher Luft- und Raumfahrtkongress 2016*, Braunschweig, 2016.

[56] P. Poisson-Quinton and L. Lepage. *Boundary Layer and Flow Control. Its Principles and Application: Survey of French research on the control of boundary layer and circulation.* Pergamon Press, New York, 1961.

[57] G. Qiao, G. Liu, Z. Shi, Y. Wang, S. Ma, and T. C. Lim. A review of electromechanical actuators for more/all electric aircraft systems. *Proceedings of the Institution of Mechanical Engineers, Part C: Journal of Mechanical Engineering Science*, 232(22):4128–4151, 2018.

[58] D. P. Raymer. *Aircraft design : a conceptual approach.* AIAA education series. American Institute of Aeronautics ans Astronautics, Washington, 2. ed. edition, 1992.

[59] J. Roskam. *Airplane Design: Part I: Preliminary Sizing of Airplanes.* DARcorporation, 1985.

[60] J. Roskam. *Airplane Design: Part II: Preliminary Configuration Design and Integration of the Propulsion System.* DARcorporation, 1985.

[61] J. Roskam. *Airplane Design: Part V: Component Weight Estimation.* DARcorporation, 1985.

[62] J. Roskam. *Airplane Design: Part VI: Preliminary Calculation of Aerodynamic, Thrust and Power Characteristics.* DARcorporation, 1985.

[63] J. Roskam and C.-T. E. Lan. *Airplane aerodynamics and performance.* DARcorporation, Lawrence, Kansas, 1997.

[64] M. Schier, F. Rinderknecht, A. Brinner, and H. Hellstern. High integrated electric machine for aircraft autonomous taxiing. In *Sixth International Conference and Exhibition on Ecological Vehicles and Renewable Energies EVER11*, Monte-Carlo, Monaco, 2011.

[65] H. Schlichting and E. Truckenbrodt. *Aerodynamik des Tragflügels (Teil II), des Rumpfes, der Flügel-Rumpf-Anordnung und der Leitwerke.* Aerodynamik des Flugzeuges. Springer, Berlin, 2., neubearb. aufl. edition, 1969.

[66] M. Schollenberger. Untersuchung zur aerodynamischen wechselwirkung elektrisch betriebener propeller und tragflächen. Master's thesis, Universitity of Stuttgart, 2017.

[67] J. Seume, S. Teichel, M. Burnazzi, M. Schwerter, C. Behr, A. Rudenko, A. Schmitz, M. Dörbaum, and C. Atalayer, editors. *SFB 880 - Efficient High Lift*, Bonn, 2013.

[68] M. Soares and F. Rebelo. *Advances in Ergonomics In Design, Usability & Special Populations Part III*. AHFE Conference, 2014.

[69] Specific Range Solutions Ltd. Parametric Specific Fuel Consumption Analysis of the PW120A Turboprop Engine. SRS-TSD-002 Rev. 1, July 2009.

[70] A. M. Stoll and G. V. Mikie. Design studies of thin-haul commuter aircraft design studies of thin-haul commuter aircraft with distributed electric propulsion. 2016.

[71] M. Strack, G. P. Chiozzotto, M. Iwanizki, M. Plohr, and M. Kuhn. Conceptual design assessment of advanced hybrid electric turboprop aircraft configurations. In *17th AIAA Aviation Technology, Integration, and Operations Conference 2017*, 2017.

[72] S. Stückl. *Methods for the Design and Evaluation of Future Aircraft Concepts Utilizing Electric Propulsion Systems*. PhD thesis, 2015.

[73] G. E. Tagge, L. A. Irish, and A. R. Bailey. Systems study for an integrated digital/ electric aircraft (idea). *NASA Contractor Report 3840*, 1985.

[74] S. H. Teichel, M. Dörbaum, O. Misir, A. Merkert, A. Mertens, J. R. Seume, and B. Ponick. Design considerations for the components of electrically powered active high-lift systems in civil aircraft. *CEAS Aeronautical Journal*, 6(1):49–67, 2015.

[75] E. Torenbeek. *Synthesis of subsonic airplane design: an introduction to the preliminary design of subsonic general aviation and transport aircraft, with emphasis on layout, aerodynamic design, propulsion and performance*. Kluwer Academic Publ, Dordrecht [u.a.], repr edition, 1999.

[76] R. Voit-Nitschmann and T. Keilig. Luftfahrzeuge. In K.-H. Grote, B. Bender, and D. Göhlich, editors, *Dubbel*, volume 2, pages 1247–1281. Springer Berlin Heidelberg, Berlin, Heidelberg, 2018.

[77] J. Wenger. Short range radar - being on the market. In *2007 European Microwave Conference*, 2007.

[78] K. Wesson and T. Humphreys. Hacking drones. *Scientific American*, 309(5):54–59, 2013.

[79] W. S. Wijesoma, K. R. S. Kodagoda, and A. P. Balasuriya. Road-boundary detection and tracking using ladar sensing. *IEEE Transactions on Robotics and Automation*, 20(3):456–464, 2004.

[80] D. Wolf. Cape air, commuter airline perspective. http://www.nianet.org/ODM/ODM%20Tuesday%20presentations%20Final/13%20Wolf%20FINAL%20Cape%20Air%20NASA%20ODM%20Conference%20deck%20v7MAR16.pdf. Accessed: 09.04.2019.

[81] O. Yalcin, A. Sayar, O. F. Arar, S. Akpinar, and S. Kosunalp. Approaches of road boundary and obstacle detection using lidar. *IFAC Proceedings Volumes*, 46(25):211–215, 2013.

A. Detailed Calculations

A.1. Take-Off and Landing Distance Calculation

The methods typically used to estimate the take-off and landing distance of an aircraft are too inaccurate for an aircraft of this configuration. Hence, calculations for these distances are presented in the following two sections. These differential equations were solved in MATLAB using the maximum take off weight (MTOW) and a standard atmosphere with a high altitude of $h = 10{,}000\,ft$.

A.1.1. Take-off Distance

The take-off distance is determined by splitting the take-off process into three parts: ground roll, transition curve and climb to 35 feet. Additionally, the ground roll is split into two parts, which considers the effect of of a one engine inoperative (OEI) scenario. First, the aircraft accelerates with all engine operative to the decision speed v_1. Then, in the second phase the aircraft accelerates with OEI to the lift off speed $v_E = v_S \cdot 1.1$. The sum of all these lengths is the take-off distance. In Figure A.1, the forces for the ground roll are shown.

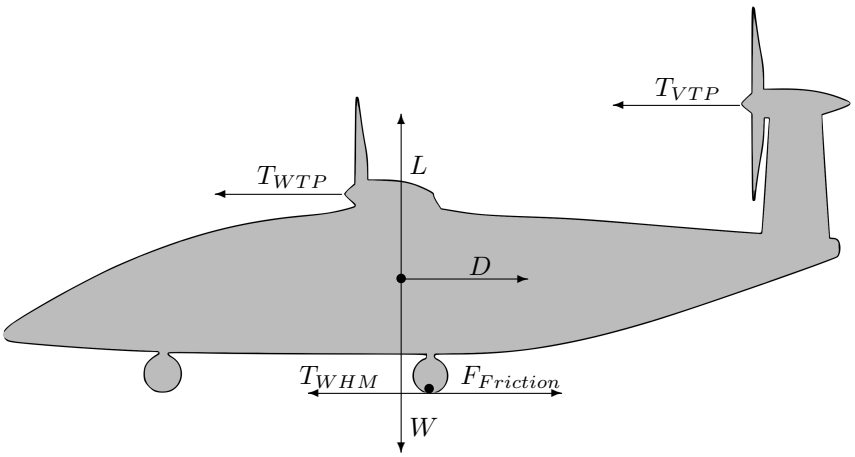

Figure A.1.: Forces during ground roll - first part of the take-off

These can be represented by the following equation:

$$F_{sum} = \sum T_{WTP} + \sum T_{VTP} + T_{WHM} - D - F_{Friction} \tag{A.1}$$

The thrust form the propellers is calculated using a simplified momentum theory. Friction force and drag are following:

$$T_{i,TO} = \sqrt[3]{(\eta_{P,TO} \cdot P_{Motor})^2 \cdot 2 \cdot \rho \cdot A_{disk}} \tag{A.2}$$

$$D = c_D \cdot \frac{\rho}{2} \cdot v^2 \cdot S \tag{A.3}$$

$$F_{Friction} = \mu_{roll} \cdot (m \cdot g - c_L \cdot \frac{\rho}{2} \cdot v^2 \cdot S) \tag{A.4}$$

The thrust provided by the WHM is given by the torque provided by the electric motor, which must be less than the frictional force provided by the brakes:

$$T_{WHM} = \frac{M_{WHM}}{r_{tyre}} \leq \mu_{break} \cdot (m \cdot g - c_A \cdot \frac{\rho}{2} \cdot v^2 \cdot S) \tag{A.5}$$

After the integration of these equation from 0 to v_1 and v_1 to v_E the ground roll (gr) distance is defined as follows:

$$l_{gr,1} = \int_0^{v_1} \frac{v \cdot m}{F_{sum,AEO}} dv \qquad l_{gr,2} = \int_{v_1}^{v_E} \frac{v \cdot m}{F_{sum,OEI}} dv \tag{A.6}$$

For the second phase of the take-off distance, the transition curve (tc), the equations are as follows:

$$v_R = 1.15 \cdot v_E \qquad R = \frac{v_R^2}{(n-1) \cdot g} \tag{A.7}$$

$$l_{tc} = R \cdot sin(\gamma_{tc}) \tag{A.8}$$

The last part of the take-off is the initial climb (ic) to 35 feet:

$$h_{tc} = R \cdot (1 - cos(\gamma_{tc})) \tag{A.9}$$

$$l_{ic} = \frac{h_{35ft} - h_{ct}}{tan(\gamma_{tc})} \qquad \forall \quad h_{tc} < h_{35ft} \tag{A.10}$$

The take off distance is then:

$$l_{TOD} = l_{gr,1} + l_{gr,2} + l_{tc} + l_{ic} \tag{A.11}$$

The decision speed v_1 is needed to find the balanced field take-off length. Therefore the aircraft must stop in the same distance as the TOD. The acceleration stop (AS) after one engine has failed needs to be calculated, whereby a braking force is applied to the wheels:

$$F_{break} = \mu_{break} \cdot (m \cdot g - c_{L,break} \cdot \frac{\rho}{2} \cdot v^2 \cdot S) \tag{A.12}$$

$$l_{gr,stop} = \int_{v_{Auf}}^{0} \frac{v \cdot m}{-(F_{break} + D)} dv \tag{A.13}$$

$$l_{AS} = l_{gr,1} + l_{braking} \leq l_{TOD} \tag{A.14}$$

A.1.2. Landing Distance

The detailed calculation of the landing distance is explained in the following section. To determine the obstacle clear distance (OCD) at $35\,ft$ it is necessary to know the height of the aircraft above the ground when landing starts. Therefore the radius $R_{landing}$ and the height $h_{tc,landing}$ of the transition curve is needed, which is defined as:

$$R = \frac{v_{abf}^2}{(n-1) \cdot g} \qquad h_{tc,landing} = R \cdot (1 - cos(\gamma_{tc,landing})) \tag{A.15}$$

The first segment l_{OCD} and the transition curve $l_{tc,landing}$ is defined by:

$$l_{OCD} = \frac{h_{35ft} - h_{tc,landing}}{tan(\gamma_{tc,landing})} \qquad l_{tc,landing} = R \cdot sin(\gamma_{tc}) \tag{A.16}$$

The braking distance is similar to the ground roll of the Take-off. As explained in 4.1 reverse thrust can be used as an additional force to decelerate. It is assumed that 60 % of the thrust could be used as reverse thrust [76]. In the following equations the forces during ground roll braking are defined:

$$F_{sum,landing} = -D - F_{break} - \sum T_{reverse} \quad (A.17)$$

$$T_{i,reverse} = \eta_{RT} \cdot T_{i,TO} \quad (A.18)$$

$$D = c_{D,landing} \cdot \frac{\rho}{2} \cdot v^2 \cdot S \quad (A.19)$$

$$F_{break} = \mu_{break} \cdot (m \cdot g - c_{L,break} \cdot \frac{\rho}{2} \cdot v^2 \cdot S) \quad (A.20)$$

After integration from v_{Auf} to 0 to ground braking distance is defined as:

$$l_{gr,break} = \int_{v_{Auf}}^{0} \frac{v \cdot m}{F_{sum,landing}} dv \quad (A.21)$$

$$l_{LD} = l_{OCD} + l_{tc,landing} + l_{gr,break} \quad (A.22)$$

A.2. Twist, Circulation and Lift Distribution

The lift distribution is designed using the Prandtl lifting-line theory. In order to reach maximum efficiency in cruise and reduce induced drag, an elliptical circulation distribution, $\gamma(\eta)$, is chosen for this operating point, which is a function of the dimensionless position on the wing $\eta = \frac{y}{b/2}$. This is achieved by twisting the wing. With a given circulation distribution and a given chord length distribution, the theory supplies the twist of the wing, $\alpha_g(\eta)$, and a lift distribution, $C_l(\eta)$. The taper ratio is chosen to increase the maximum lift coefficient of the whole wing $C_{L,max}$ at take-off and landing. The detailed distribution of twist, circulation and lift for design pint $C_L = 0.5$ and stall $C_L = 1.25$ without high lift system are shown in Table A.1 and Figure A.2, with $A = 13$ and $\lambda = 0.7$.

η	0.0000	0.1951	0.3827	0.5556	0.7071	0.8315	0.9239	0.9808	1
α_g [°]	5.70	5.90	5.91	5.69	5.18	4.40	3.35	2.08	0
γ	0.0245	0.0240	0.0226	0.0204	0.0173	0.0136	0.0094	0.0048	0
C_l	0.541	0.564	0.565	0.540	0.486	0.401	0.286	0.150	0
γ	0.060	0.058	0.055	0.051	0.045	0.038	0.030	0.017	0
C_l	1.32	1.37	1.37	1.34	1.27	1.13	0.91	0.54	0

Table A.1.: Twist, circulation and lift distribution at design (top) and stall (bottom) operating point

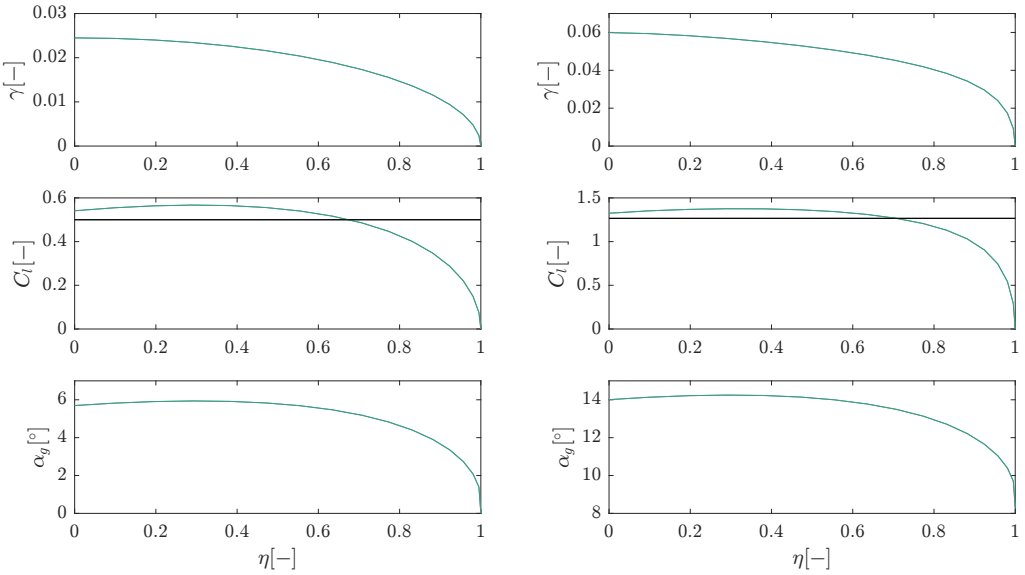

Figure A.2.: Circulation, lift and twist distribution at cruise (left) and stall (right) operating point (green), C_L (black).

A.3. Zero-Lift Drag Coefficient

The zero-lift drag coefficient of the aircraft $C_{D,0}$ is estimated by the Class II Method by Gundmundsson [29] to $C_{D,0} = 0.019$. Table A.2 shows the different shared which contribute to the zero-lift drag coefficient.

	Drag Area $\frac{D}{q}$ $[m^2]$
fuselage surface	0.118
V-tail surface	0.059
Fuselage Upsweep	0.0157
Cockpit Windshield	0.006
Wing	0.103
$\frac{Sum_{DragArea}}{S_{ref}} = C_{D,0}$	0.019

Table A.2.: Summands for calculating $C_{D,0}$.

A.4. Power Requirements for Coanda System

For characterizing the momentum and the power of the coanda jet the dimensionless momentum coefficient C_μ [56] and the power coefficient C_{Power} [14] are introduced.

$$C_\mu = \frac{F_j}{q_\infty S_{ref}} = \frac{U_j \dot{m}_j + (p_j - p_a)A_j}{\frac{1}{2}\rho_\infty U_\infty^2 S_{ref}}; \qquad C_{Power} = \frac{P_j}{\frac{1}{2}\rho_\infty U_\infty^3 S_{ref}} \tag{A.23}$$

These equations use following variables: Thrust of the jet F_j, stagnation pressure q_∞, density ρ_∞, reference wing area S_{ref}, flight velocity U_∞, jet velocity and jet mass flow rate U_j and $\dot{m}_j$, area of the jet outflow A_j, ambient pressure and jet pressure p_a and p_j, power of the jet P_j. At subsonic speeds the pressure difference, $(p_j - p_a)$, can be neglected.
Burnazzi [14] has investigated the effect of the jet height h_j on C_μ and C_{Power} keeping the maximum lift coefficient constant at $C_{l_{max}} = 5.0$. With an increase in jet height the required C_μ increases but C_{Power} deceases due to a decrease in jet velocity, U_j. The jet height and mass flow are optimized for high lift coefficients and a low required power according to Burnazzi [14]. The jet height is $h_j = 0.18\%$ chord length, which results in $C_\mu = 0.05$ and $C_{Power} = 0.055$ when $C_{l_{max}} = 5.0$ is fixed. Adding the effect of the flexible droop nose, the lift coefficient can be increased to $C_{l_{max}} = 6.0$, [14].
With equation A.23 for C_{Power} and the conditions at take off, the power of the jet is calculated to $P_j = 33.2kW$. With an assumed efficiency of the compressor of $\eta_{comp} = 0.7$ the electrical Power results to $P_{el} = 47.4kW$.

A.5. Moment Balance at Take-Off

Table A.3 shows the components for the moment balance at take-off with wing tip propeller inoperative and V-tail propeller at maximum power, which is the critical operating point for the pitch moment. With an angle of attack at the elevator of $\alpha_{el,TO} = 10°$ during take-off the thrust vector is angled downwards which reduces the lever arm for the torque generated by the propeller.
The elevator has a lift coefficient of $C_{l,TO} = -1.3$ (see Section 5.4.3) and at a take-off velocity of $v_{TO} = 34m/s$ and a tail-unit lever arm of $r_{x,tail} = 6.6\,m$ the moment generated by the lift of the elevator is $26.9 \cdot 10^3\,Nm$. The propellers at the V-tail generate $F_{p,tail} = 15 \cdot 10^3\,N$ in this OEI configuration. With a lever of $r = 2\,m$ due to the trim with $\alpha_{el,TO} = 10°$ at take-off, the torque generated by the propellers at the rear is $-30.0 \cdot 10^3\,Nm$. With this calculation, the moment balance for the most critical situation is shown.

Position	Moment $[10^3\,Nm]$
Moment Wing	-15.1
Lift Wing	6.8
Drag Wing	8.3
Moment Elevator	2.5
Lift Elevator	26.9
Drag Elevator	0.6
Thrust WTP	0
Thrust V-tail Prop	-30.0

Table A.3.: Moment equilibrium during Take-Off